3D RESERVOIR SIMULATION OF A HYDRAULICALLY FRACTURED VERTICAL GAS WELL USING THE EMBEDDED DISCRETE FRACTURE MODEL (EDFM)

A Thesis

by

SAMUEL RENE ORTA

Submitted to the Office of Graduate and Professional Studies of
Texas A&M University
in partial fulfillment of the requirements for the degree of

MASTER OF SCIENCE

Chair of Committee,	John Killough
Committee Members,	Eduardo Gildin
	Stratos Pistikopoulos
Head of Department,	Stratos Pistikopoulos

August 2017

Major Subject: Energy

ABSTRACT

According to the 2017 outlook on energy conducted by the EIA, the production of natural gas from shale reservoirs is expected to increase by 2040. This increase is dependent on multiple factors like technology, resources, and market conditions. In order to meet production increases, improvements in industry practices must happen in order to achieve better economic development of these reservoirs. One of the primary tools used in economic development is reservoir simulation.

However, modeling and simulating low permeability reservoirs, like shale, can be complex due to the presence of natural fractures. Knowing that fractures have a significant role in the total recovery of a field, modeling the influence of these fractures is of utmost importance. There are two common methods used to model naturally fractured reservoirs, the dual continuum model and the discrete fracture model.

In this study, an embedded discrete fracture model (EDFM) was used to simulate and match a hydraulically fractured vertical gas well in the Barnett Shale in 3D. EDFM was proposed by Li and Lee (2008) to couple the dual continuum model with the discrete fracture model to take advantage of both methods. The results show that EDFM can be validated and can be an efficient tool for future reservoir simulation. In addition, a parametric study was conducted to visualize how fracture orientation and fracture density impact fluid flow. It was concluded that fracture orientation plays an important part in fracture connectivity, which is a result of fracture orientation. If the fractures are highly connective, the better the well performance. The same was seen with fracture density, an increased fracture density leads to better well performance.

DEDICATION

To my beloved parents, Linda and Sam, my lovely sister Samantha, and all my family and friends for their unconditional love, patience, support, and encouragements.

ACKNOWLEDGEMENTS

I am sincerely grateful to my advisor, Dr. John Killough, for his invaluable advice and excellent supervision throughout my Master's study. I would also like to express my deepest gratitude to the other members of my thesis committee and contributing faculty, Dr. Eduardo Gildin, Dr. Carlos Dengo, Dr. Mukul Bhatia, and Dr. Stratos Pistikopolous, for their time and effort to serve on my committee and review my work.

I greatly acknowledge Dr. Valentini Pappa and Jeff Sammons with The Texas A&M Energy Institute for guiding me in the first year of the Energy program and for the work that they have put into my professional development.

I would also like to express my gratitude to Chai Zhi, a PhD candidate at Texas A&M University for his patience and guidance. Without Chai, I would not have been able to finish this project in the time that I did. To all of my friends who helped and supported me throughout my time here at Texas A&M, I am extremely grateful. My achievements would not have been possible without their help and inspiration.

CONTRIBUTORS AND FUNDING SOURCES

This work was supervised by a thesis committee consisting of my advisor, Dr. John Killough of the Department of Petroleum Engineering, Dr. Eduardo Gildin of the Department of Petroleum Engineering, and Dr. Stratos Pistikopolous of the Department of Chemical Engineering and Director of the Texas A&M Energy Institute.

The Matlab executable discussed in Section 3 was provided by PhD Student Chai Zhi. The analyses of the discrete fracture network depicted in Section 4 was conducted by Master's student Guillaume Lostis. All other work for the thesis was completed independently by Sam Orta.

This work was made possible by the Texas A&M Veterans Association under the Hazlewood Exemption Act.

TABLE OF CONTENTS

LIST OF FIGURES

LIST OF TABLES

1. INTRODUCTION

1.1 FLUID FLOW IN FRACTURED RESERVOIRS

Natural gas production from unconventional shale gas reservoirs accounted for only about 1% of total U.S. energy production in the year 2000. Currently natural gas production accounts for nearly 27% of total U.S. energy production with projection to increase to 40% by 2040, according to the reference case of the EIA's Annual Energy Outlook of 2017 seen in Figure 1. Two-thirds of the U.S. total natural gas production is projected to come from unconventional shale gas reservoirs by 2040, seen in Figure 2. If the reference case holds, about 26% of all U.S. energy production will come from unconventional shale gas reservoirs. However, this production growth is dependent on technology, resources, and market conditions. Nonetheless, America is in the midst of the "Shale Revolution" and the term unconventional is becoming "conventional" (Breyer, 2012).

Advances in oil and natural gas production technologies, particularly hydraulic fracturing and horizontal drilling, gave the opportunity for this shale revolution. However, America is also in the midst of "do more with less" due to current market conditions. Due to the increase in expected natural gas production in shale reservoirs, improvements in industry practices must happen in order to get better economic development in shale reservoirs with less. In order to select the best stimulation strategy, the accuracy of reservoir characterization and simulation studies in low permeability rocks needs to be improved. This requires better monitoring of well completion and overall improvements

in simulation strategies. However, the presence of natural fractures in shale formations can make fluid flow simulation challenging. When a reservoir is hydraulically fractured, complex fracture networks between the natural and hydraulic fractures are created, making the predictability of fluid flow difficult (Moinfar, 2013).

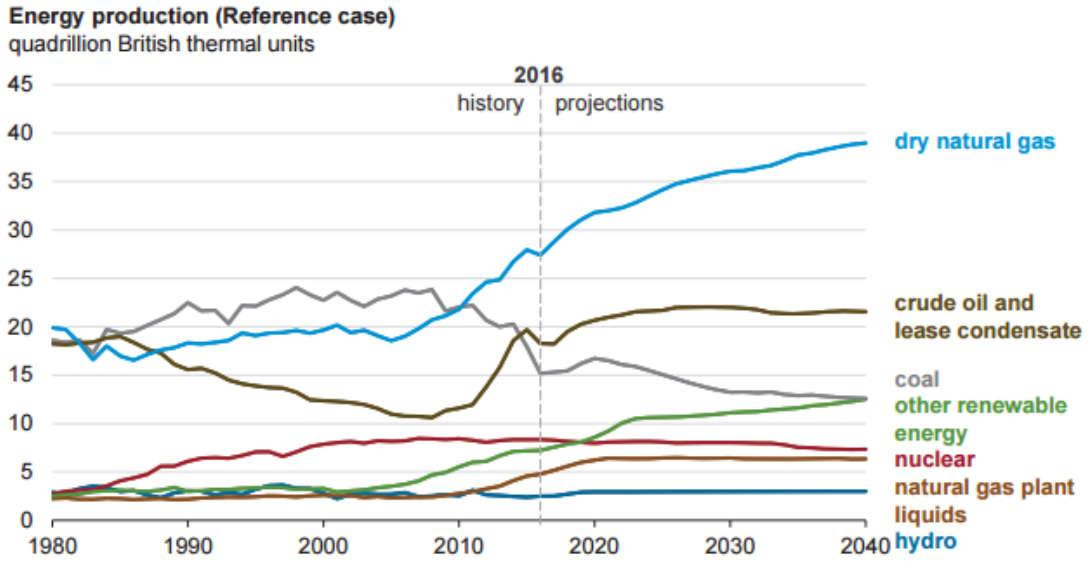

Figure 1: The reference case for total U.S. Energy production of different resources projected until 2040. Reprinted from (U.S. Energy Information Administration, 2017)

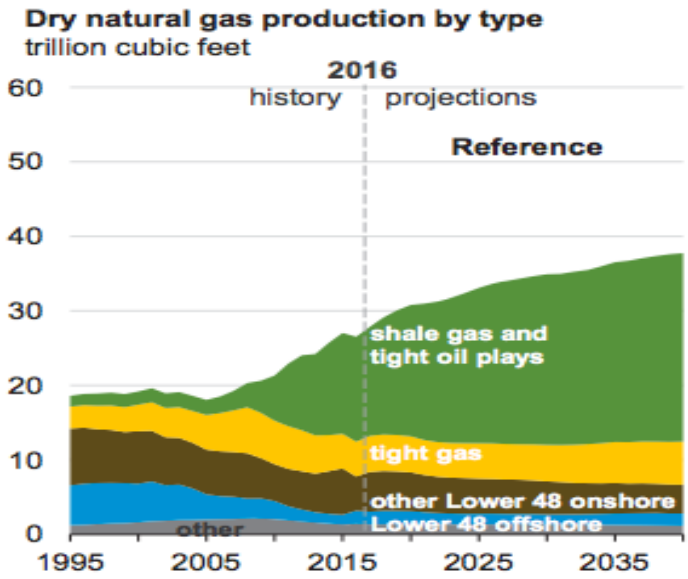

Figure 2: The reference case of dry natural gas production by type in trillion cubic feet projected until 2040. Reprinted from (U.S. Energy Information Administration, 2017)

Fractures introduce a direction of maximum and minimum permeability, which may ultimately affect the total recovery of the reservoir (Xu, 2015). In addition, the efficiency of a production strategy may highly depend on the fracture network connectivity, which is not easy to directly measure (Lee et al. 1993, cited in Xu, 2015). Furthermore, the high capillary difference between fractures and the matrix may cause differences in recovery performance between fractured reservoirs and non-fractured reservoirs.

Seeing that the presence of fractures has a significant role in production, it is of utmost importance to accurately model the influence of these fractures in order to get better economic development in shale reservoirs. Several approaches, like the dual

continuum models or discrete fracture models, have been proposed to model fractured reservoirs and extensive work has been done to improve these models (Xu, 2015).

Dual porosity and dual permeability models were proposed to model naturally fractured reservoirs. Presently, they are still the most commonly used modeling approaches. These approaches discretize the matrix and fracture into two different domains, storage and fluid flow, respectfully. The two domains are then coupled through a transfer function. This approach is simple to implement in commercial simulators and transforms a heterogeneous problem into a homogeneous one. However, although these dual continuum approaches are very efficient, they are a very simplistic representation of the complex fracture network in the reservoir. An upscaling of fracture characteristics makes these approaches inadequate for solving different fluid flow problems in fractured reservoirs. Nonetheless, they are very efficient for reservoirs with a large number of inter-connected small-scale fractures (Moinfar, 2013).

Discrete Fracture Models (DFMs), however, have been developed to simulate naturally fractured reservoirs more accurately. DFMs, have not been widely used in the industry for field-scale reservoir simulation studies, even though they give more accurate representations of flow in fractured reservoirs than conventional methods. In this type of model, each fracture is explicitly described as a 2D interface. A large number of grid blocks are required near the fracture, which results in increased computational time. In addition, most DFM approaches require an unstructured grid to conform to the complexity of the fractures assigned to the domain of interest. Generation of such a grid for an arbitrary fracture network can be time lengthy and challenging.

To take advantage of both the dual continuum and discrete fracture models, Lee et al. (2000, 2001) presented an approach for simulating fluid flow in fractured reservoirs called the embedded discrete fracture model (EDFM). This type of model honors DFMs by discretizing each fracture explicitly while borrowing the dual-medium concept from the dual continuum models.

There have been several projects focused on using the Embedded Discrete Fracture Model to simulate fractured reservoirs. Li and Lee (2008) implemented this approach for vertical fractures. Moinfar et al. (2013) extended the EDFM to 3D simulations using GPAS reservoir simulator, a fully-implicit in house compositional simulator at the University of Texas, and implemented the model for obliquely dipping fractures, which are common in NFRs. Later, Shakiba (2014) implemented the EDFM in another compositional simulator (UTCOMP) and a chemical simulator (UTGEL) to investigate several recovery mechanisms in fractured reservoirs. Xu (2015) implemented EDFM in a chemical EOR simulator, (UTCHEM), to study complex EOR processes in fractured reservoirs. Xu (2015) also implemented the EDFM into a commercial simulator, Eclipse, to prove its compatibility with existing reservoir simulators and to generate a general procedure so EDFM is more powerful and more widely used. Recently, Lostis (2016) implemented EDFM into another commercial simulator, Landmark's Nexus, using 2D simulations to match the production history of a vertical hydraulically fractured well. This expanded the range of problems the EDFM can solve in field scale.

This research is a field scale study intended to expand the work of Lostis (2016) by creating a 3D EDFM of the same vertical hydraulically fracture well and conducting

multiple simulations to understand the impact that fracture orientation, connectivity, and density have on well performance.

1.2 OBJECTIVES

Based on this, the objectives of this research are to:

1) Use EDFM to model a hydraulically fractured vertical gas well in the Barnett Shale Formation, Well Pearl Cox 6, in 3-Dimensions and match it to the production history.

2) Conduct different comparison runs to see how different fracture orientations and connectivity's affect production, along with how fracture density affects production.

In past, EDFM proved to be compatible with commercial simulations and a good modeling method to model fractured reservoirs. With EDFM being able to capture the complex fracture network while still using the efficiency of structured gridding, EDFM can produce reasonably accurate results at a much lower computational cost.

1.3 BRIEF DESCRIPTION OF SECTIONS

Section 2 presents a brief literature review of some of the proposed methods for fluid flow predictions in fractured reservoirs. This includes the dual-continuum and discrete fracture models. Section 3 discusses the principals of the Embedded Discrete Fracture Model. Section 4 gives background to the fracture network surrounding Well Pearl Cox 6. Section 5 discusses the 3D model and the results of the base and matched simulations. Section 6 discusses the sensitivity analysis done on different fracture orientations and densities. The last section, section 7, highlights key points in research and gives recommendations for future studies.

2. BRIEF REVIEW OF FLUID FLOW MODELING IN FRACTURED RESERVOIRS

The presence of fractures that have various lengths and apertures, combined with the presence of small fracture volumes, makes numerical simulation very challenging in fractured reservoirs. Several models have been proposed to model fluid flow in naturally fractured reservoirs. The two reviewed in this study are the dual continuum models and discrete fracture models. Currently, dual continuum models are the most commonly used modeling method in the petroleum industry. However, discrete fracture modeling methods are increasing in interest.

2.1 DUAL CONTINUUM MODEL

Dual continuum models are the most commonly used modeling method in the petroleum industry. The method is based on a concept originally proposed by Barenblat et al. (1960) (cited in Moinfar, 2013). It is through this concept that Warren and Root (1963) (cited in Moinfar, 2013) introduced the dual porosity model, also known as the sugar cube model. This model was first used for single-phase flow in fractured reservoirs. Since then it has advanced to model multiphase flow. The concept discretizes the reservoir into two domains, matrix and fracture, so every point within the reservoir has fracture and matrix pressures and saturations. The model presumes that the fluid flow occurs from the matrix to the fractures and then to the wells. The matrix is considered only for storage and the fractures are considered the main pathway for fluid flow. Although this is true for low permeability reservoirs, conventional reservoirs might have fluid flow in the matrix. The matrix and the fractures are then connected to each other through an exchange term that connects each fracture cell to its corresponding matrix cell in a grid block. This exchange

rate is controlled by the shape factor, which is not easy to calculate (Moinfar, 2013). Figure 3 shows an example of the sugar cube representation of a fractured reservoir. The original dual porosity model assumes that fracture intensity is uniform throughout the reservoir and hence the matrix block size is constant.

The dual-permeability model was developed, using the same concept as dual-porosity model, but would allow for matrix-to-matrix flow since the matrix domain only acts as fluid storage in the dual porosity model (Moinfar, 2014). Dual-permeability and dual-porosity models have been considered the conventional method for modeling fractured reservoirs and have been implemented in many reservoir simulators for field-scale fractured reservoir simulations. However, the dual-continuum models pose fracture uniformity, which does not capture the heterogeneity of the fracture network. Through geological studies and outcrop observations, geologists have indicated that there are occurrences of non-uniform fracture patterns owing to varying lithology, bed thickness, and stress environment. Although these models are efficient, they are insufficient for solving fluid flow problems in complex fractured reservoirs like the Barnett Shale.

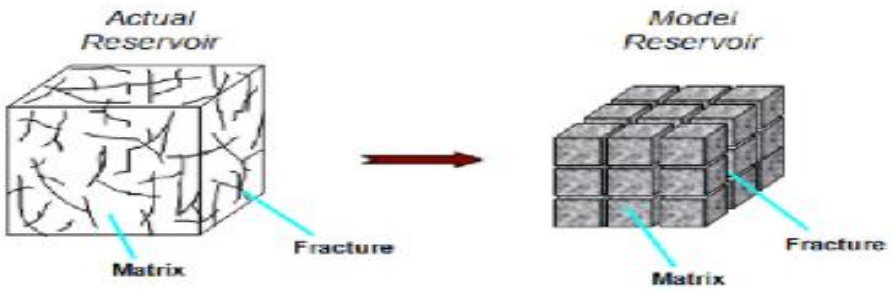

Figure 3: Representation of the sugar cube model. Reprinted from (Moinfar, 2013).

2.2 DISCRETE FRACTURE MODEL

Outcrop characterization studies have shown that natural fractures vary substantially in height, length, and aperture, as well as spacing and network connectivity, thus highlighting a large discrepancy between reality and the uniformity inherent in dual continuum model assumptions. Hence, discrete fracture models (DFMs) were developed to reduce the number of non-physical abstractions built into the dual continuum models. These models create more realistic representations of the fractured reservoir than dual-continuum models, but most of these models rely on unstructured grids to conform to the geometry and the location of the fracture network. Compared to dual porosity models, DFMs offer several advantages. They account explicitly for the effect of individual fractures on fluid flow. In addition, they are not excessively constrained by grid defined fracture geometries; so, the fracture model is easily adaptable and updatable. Moreover, the specification of the fluid exchange between matrix and fracture is more straightforward since it depends directly on the fracture geometry and any assigned relative permeability and capillary pressure functions.

However, two disadvantages are that, in general, DFMs are numerically difficult to implement and are computationally expensive. Further, one must be able to identify the locations and orientations of the discrete fractures for the model to be realistic. Figure 4 depicts a 2D example of a fracture network defined in a physical domain. For this example, the matrix is represented by 2D control volumes and the fractures are represented by 1D control volumes. As shown in the Figure 4, each control volume is associated with a node.

Although the fracture thickness is not represented in the grid domain, it is included in the computational domain for flow-rate evaluation.

To accurately capture the complexity of a fractured reservoir, it is usually necessary to use an unstructured discretization scheme. However, generation of such a grid for an arbitrary fracture network can be a substantial challenge.

With these challenges in mind, Lee at al. (2001) proposed a distinctly different DFM for simulating fluid flow in NFRs. Their proposed model uses a conventional structured grid to represent the matrix and introduces additional fracture control volumes that are connected to the matrix through a communication channel called non-neighboring connections. Thus, the challenges associated with unstructured gridding are avoided entirely. This approach is called the Embedded Discrete Fracture Model.

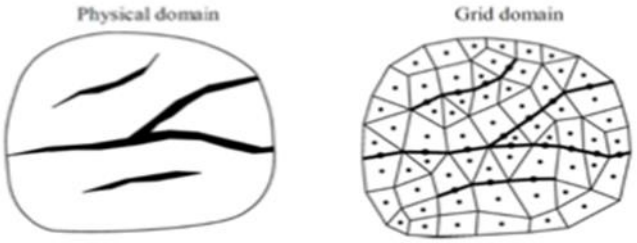

Figure 4: Representation of a discrete fracture model. It can be seen that the gridding surrounding the fracture is unstructured. Reprinted from (Moinfar, 2013).

3. FUNDAMENTALS OF THE EMBEDDED DISCRETE FRACTURE MODEL (EDFM)

Accurate modeling and simulation of naturally fractured reservoirs has proved to be challenging due to permeability variations and contrasts. Two methods have been reviewed to model naturally fractured reservoirs, dual continuum models and discrete fracture models. Although very successful, dual continuum approaches are not efficient for large-scale fracture modeling or capturing the influence of fracture connectivity. On the other hand, recent discrete fracture modeling technologies suffer from large computational times and the industry has not quite utilized this approach, even though it gives more accurate representations of fractured reservoirs than dual continuum models. The embedded discrete fracture model used in this research combines the simplicity of the dual continuum models with the complex capturing ability of the discrete fracture models.

In this section, the fundamentals of EDFM will be discussed, along with how it was implemented into the reservoir simulator, Landmark's Nexus.

3.1 OVERVIEW OF EDFM

Li (2001) proposed The Embedded Discrete Fracture Model (EDFM) and it was implemented by Li and Lee (2008) for simulating flow in naturally fractured reservoirs. The concept discretizes the reservoir into two domains just like the dual medium concept, matrix and fracture. The model uses a structured grid to represent the matrix and introduces additional fracture control volumes by computing the intersection of fractures with the matrix grid. The same grid block sizes are used for both matrix and fracture domains, however, there is no need for both grid block sizes to be the same in this

approach. The matrix and intersecting fractures are then connected by non-neighboring connections (NNCs), which provides fluid communication between the two domains. All of these computations are calculated by a preprocessing code that is then implemented into the reservoir simulator.

3.2 FRACTURE – MATRIX INTERSECTION

As mentioned above, the intersection of all fractures with the matrix grid should be computed in order to couple the matrix and fracture domains. Figure 5 shows possible intersections between a single matrix grid cell and a fracture. The specific locations of these intersections are needed for calculating the connection between the two domains. For vertical fractures, the intersection between the vertical fractures and a matrix cell is usually rectangular which can be seen in Figure 5a. For an intersection between an inclined fracture plane and a matrix cell, the intersections are polygons with 3,4,5 or 6 corners. These are triangles, quadrilaterals, pentagons, or hexagons, respectively.

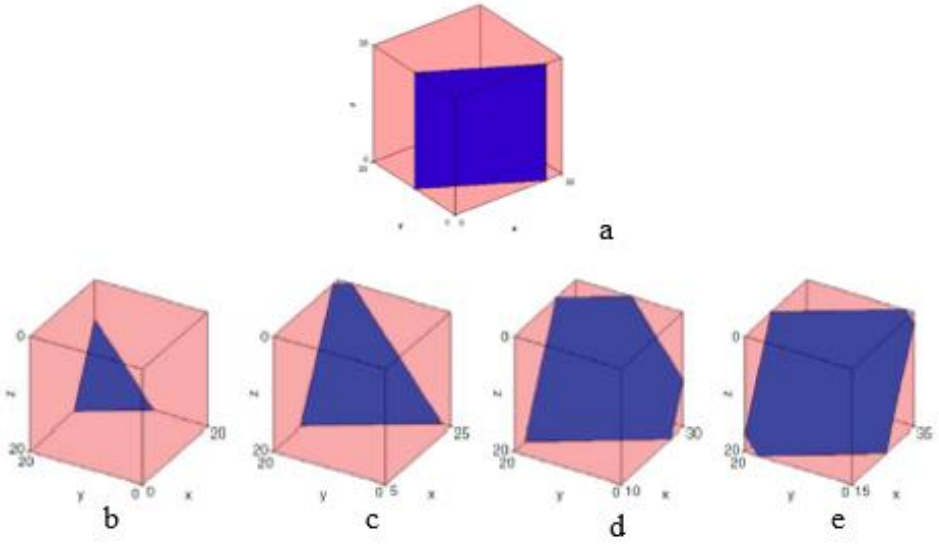

Figure 5: Possible intersections between a single matrix grid cell and a fracture. (a) represents vertical fracture intersection with cell. (b) - (e) represent inclined fracture intersections with cell. Reprinted from (Moinfar, 2013).

A fracture cell should be defined in the fracture domain corresponding to each gridblock containing a segment of a fracture plane. To help illustrate this concept, an example from Moinfar (2013) will be used. Figure 6 is a 10 x 10 x 2 matrix grid with 2 arbitrary fractures with inclination at 60 and 75 degrees. The cell dimensions for the matrix are 20 x 20 x 20 ft. in all directions. Both fractures penetrate the entire height of the reservoir. These fractures are represented by 2-D surfaces and the surfaces of these fractures are in contact with individual matrix grid cells, which can be seen in Figure 7. The matrix cells that are intersecting with the fractures in the top layer are shown on the left and the matrix cells that are intersecting with the fractures in the bottom layer are shown on the right.

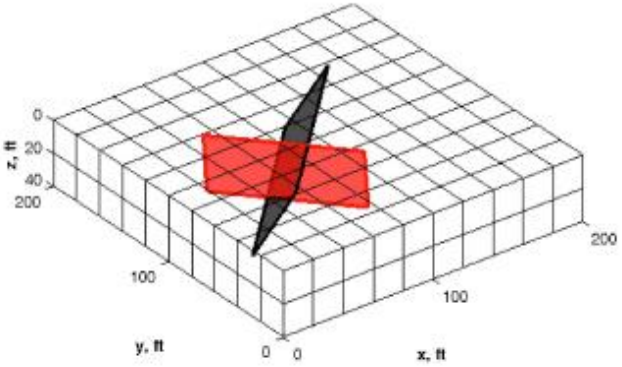

Figure 6: Illustration of how the 2D fracture surfaces intersect with 3D matrix grid. The matrix grid is 10 x 10 x 2. Reprinted from (Moinfar, 2014).

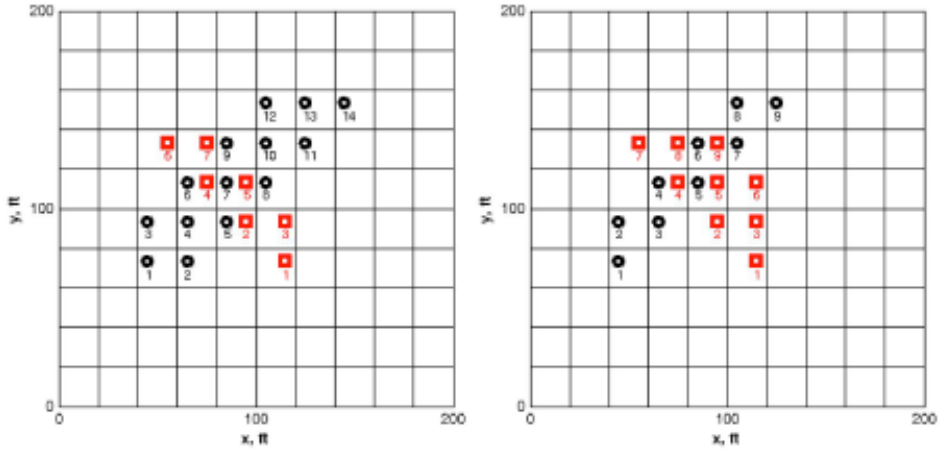

Figure 7: Illustration displaying how the 2D fracture surface would be represented when combined with the matrix grid for each layer for Figure 6. The top layer is represented on the left. The bottom layer is represented on the right. Reprinted from (Moinfar, 2014).

As shown, a matrix grid cell may contain more than one fracture segment, all which should be considered separately in the fracture domain. Once the intersection of the matrix and fractures are computed, there needs to be some sort of fluid communication between the fractures and the matrix since they are on separate computational domains.

The mass balance equations have no fluid connection between them, so there is a need to define the non-neighboring connections (NNC) for EDFM (Moinfar, 2013). That is, each grid-block in the numerical model can communicate with any other grid-block through an NNC (Moinfar, 2013).

3.3 NON-NEIGHBORING CONNECTIONS AND FORMULATIONS

In order for the matrix and fracture cells to have fluid communication, there has to be non-neighboring connections (NNCs) between the cells. NNCs allow grid-blocks to communicate between each other. There are three types of NNCs required for appropriate communication:

- -Type I: NNC between a fracture cell and neighboring matrix grid-block. If a fracture goes through a certain matrix cell or grid block, that intersection between the two needs fluid transfer because fluid will flow through the matrix and the fracture.
- -Type II: NNC between two intersecting fractures. When fractures intersect each other, fluid exchanges between the two. So, it is important to have fluid communication between the two intersections.
- -Type III: NNC between two cells of an individual fracture line. An individual fracture will obviously have fluid flow running though it and it will most likely pass through multiple cells in the model. Therefore, there is a need to have communication between the cells that the fracture passes through.

All three NNC types can be seen in Figure 8.

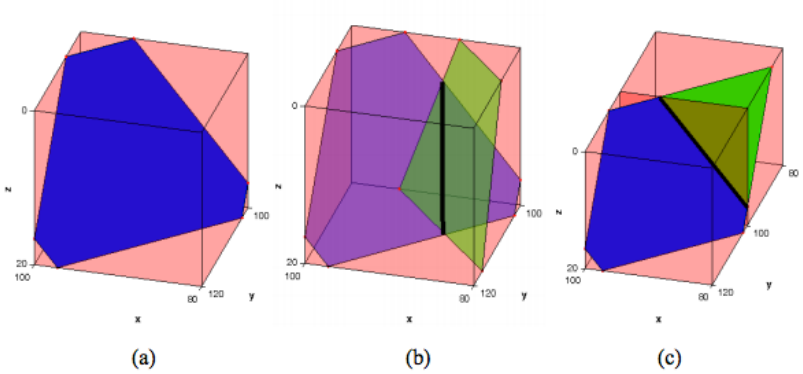

Figure 8: Illustration displaying all three types of Non-Neighboring Connections (NNCs). (a) Type 1 (b) Type 2 (c) Type 3. Reprinted from (Moinfar, 2013).

These three types of NNC's need to be implemented into the mass balance equations that will be added to Landmark's Nexus. These equations numerically calculate the connections between the fractures and the matrix cells as well as the transmissibility of the NNCs. The variables A^{nnc}, k^{nnc}, and d^{nnc} are the area open to flow, the harmonic average of permeability, and the characteristic distance, respectively and are used to determine the transmissibility factor. The transmissibility factor represented by Eq (1) needs to be calculated for each type of NNC in order to have accurate fluid communication between the fracture and the matrix.

$$\frac{(A^{NNC}\, x\, k^{NNC})}{d^{NNC}} \qquad \text{Eq. 1}$$

These calculations have been calculated and implemented into the pre-processing code developed by Chai Zhi, a PhD candidate at Texas A&M University. The pre-processing code developed by Chai had great influence from Moinfar (2013).

3.4 EDFM PRE-PROCESSING CODE - IMPLEMENTATION

The implementation of the EDFM consists of two parts: 1) pre-processing of the fracture network over an arbitrary grid to provide the required data for reservoir simulation and 2) implementation of NNCs, transmissibility modifiers, and other necessary changes into the reservoir simulator.

The calculations of the matrix and fracture connections, depend on gridding, reservoir permeability, and fracture geometries. Since no time-varying properties like pressure and saturation are involved in the formulations, the calculations of the connecting factors in the EDFM can be independent from reservoir simulation. Chai Zhi, developed an EDFM pre-processing code to calculate all of these connection factors. The pre-processing code has been tailored to Landmark's Nexus reservoir simulator, as all simulators handle the input of NNCs differently.

The pre-processing code is a Mat-lab executable that reads a text file and outputs .dat files that are used in the property files section of the case file in the Nexus software. The user manually enters the inputs for the text file. The text file should include:

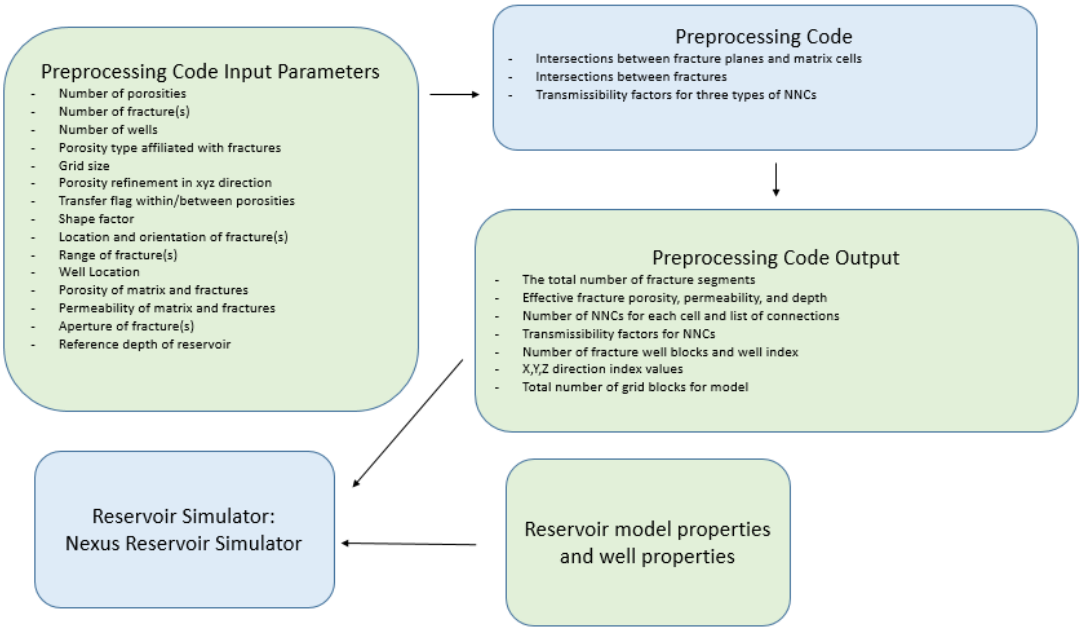

Figure 9: Work flow of how the preprocessing code is implemented into reservoir simulation.

In Figure 9, the preprocessing code output files will be a part of the property files section in the case file that specifies the data input of a simulation run in Landmark's Nexus reservoir simulator. Now that the fundamentals of the embedded discrete fracture model (EDFM) has been discussed, we can begin talking about the fracture network around pearl cox 6.

4. FRACTURE NETWORK AROUND PEARL COX 6

Pearl Cox 6 is a vertically fractured well located within the core part of Newark East Field, in the northern portion of the Fort Worth Basin, seen in the Figure 10. In 2001, a huge hydraulic-fracture diagnostic project was undertaken by Devon Energy that integrated fracture-diagnostic technologies, like tilt-meter mapping and microseismic mapping, to approximate the effective fracture network in the area (Mayerhofer, 2006). Pearl Cox 6 was fracture treated and mapped during this diagnostic project. The data gathered during this diagnostic provided a clearer understanding of the highly complex fracture behavior in the Barnett Shale Formation. Typically, fractures can be classified as simple, complex or very complex. Because of the presence of natural fractures, the fracture network in the Barnett is more likely to look like the very complex fracture description.

In this chapter, a brief background of the Barnett Shale will be discussed to fully understand the formation that will be simulated, along with how the approximated fracture network used in this project was created for the EDFM. Understanding the fracture growth is very important not only to understand fluid flow patterns but also to optimize well location and spacing. The microseismic events provided a completely new understanding of the fracture growth in this area.

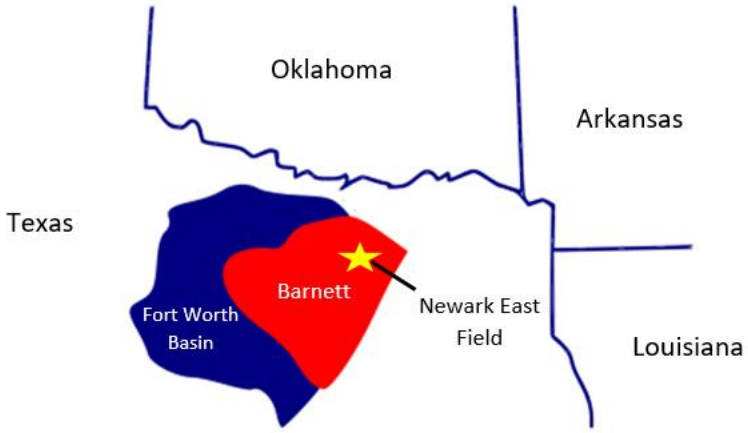

Figure 10: General location of Newark East Field.

4.1 THE BARNETT SHALE FORMATION

The Barnett Shale is a Mississippian aged marine shelf deposit that unconformably lies on the Ordovician-age Viola limestone/Ellenburger group and is conformably overlain by the Pennsylvanian-aged Marble Falls Limestone seen in Figure 11 (Scott et al., 2005). The Barnett Shale within the Fort Worth Basin ranges from 200 to 800 ft. in thickness and is approximately 500 ft. thick in the core of the field. The production part behind the shale formation is a black, organic rich shale composed of fine grained, nonsiliciclastic rocks with extremely low permeability, ranging from .00007 to .005 md. The formation is abnormally pressured, and hydraulic-fracture treatments are necessary for commercial production because of low permeability.

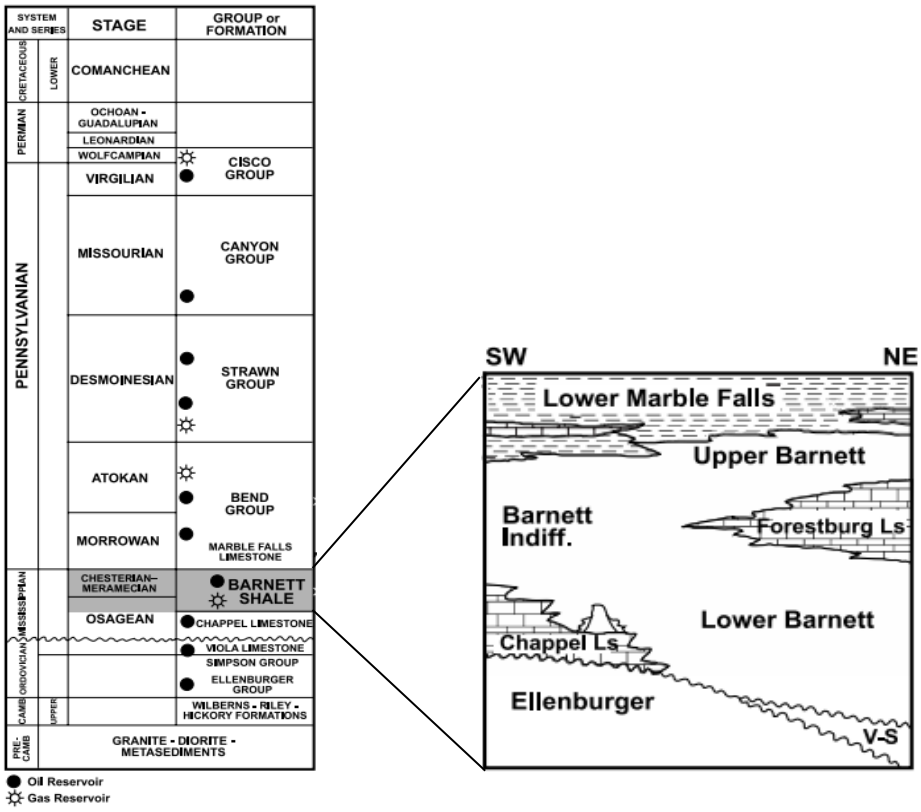

Figure 11: Stratigraphy of core part of the Barnett Shale. Reprinted from (Scott, 2005)

4.2 MICROSEISMIC OF PEARL COX 6

As mentioned above, Pearl Cox 6 was one of many wells in the Barnett Shale mapped with fracture-mapping technologies when the fracture diagnostic project took place in 2001(Fisher, 2005). The mapping technologies provided a detailed trend of how the effective fracture network propagated throughout time allowing for an approximation of the fracture network orientation, height, length, and width. Several fracture-mapping technologies are available to develop an accurate image of the fracture growth. These are Surface tiltmapping, downhole tiltmapping, and microseismic mapping.

Surface tiltmapping is a tool used to map the deformation caused at the surface of the Earth by hydraulic fractures or dislocations in the subsurface. Downhole tiltmapping is similar to surface tiltmapping but used for a different application. The tiltmeter instrument's resistance to stress is strengthen and placed in offsetting wellbores where hydraulic fracture dimensions can be determined. Microseismic mapping measures the location of microearthquakes, which result from the placement of a hydraulic fractures. These slippages are detected by vertical arrays of five to 12 sensitive listening devices, called geophones, placed in an offsetting wellbore.

In order to develop an accurate image of the fracture growth, a combination of these technologies would be best like Fisher (2005) incorporated, but surface tiltmapping and downhole mapping information is not at hand for this project. All information about the fracture network and growth available for the project are the microseismic images used by Lostis (2016). Figure 12 and Figure 13 are completed microseismic event images of the Lower Barnett Shale Formation after a 7-hour time lapse used by Lostis (2016). Figure 12 is given in horizontal plane view and Figure 13 is viewing the events transversely to the N45E. These images show that the hydraulic fracture growth is complex in the Barnett Shale, but a general trend is distinguishable.

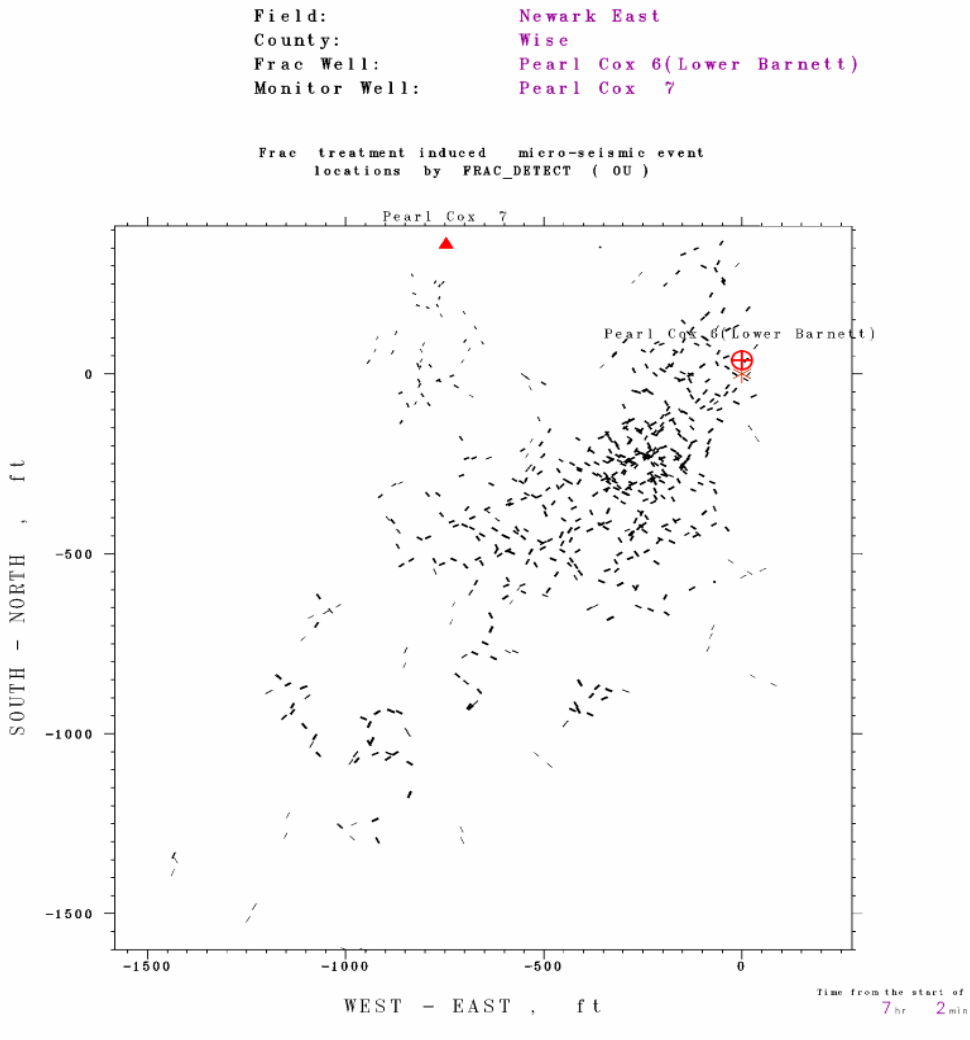

Figure 12: Completed microseismic event images of the Lower Barnett Shale given in horizontal plane view (top view). Adapted from (Lostis, 2016).

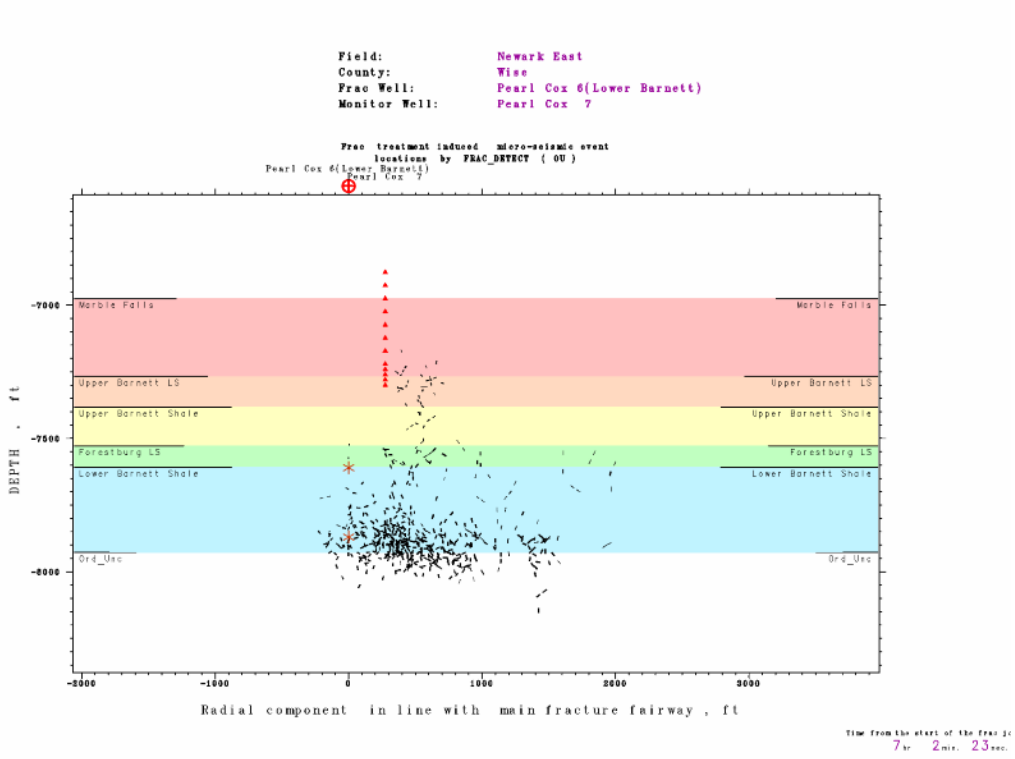

Figure 13: Completed microseismic event images of the Lower Barnett Shale given in transverse view (side view) N45E. Adapted from (Lostis, 2016).

The information about the extent of the microseismic events were derived from Lostis (2016) and Mayerhofer et al. (2006). From the figures above, it can be seen that there are two sets of fractures. One set striking northwest to southeast, and the other set striking northeast to southwest. Through Lostis (2016) and Mayerhofer et al. (2006), it is known that the existing natural fractures are striking northwest to southeast and the hydraulic fractures are striking northeast to southwest. Figure 12 shows that the fracture network propagated asymmetrically in the southwest direction, in relation to well Pearl Cox 6 and there was no activity in the northeast direction. Pearl Cox 7, which is the monitor well at this location, was located in a position where it should have detected

growth to the northeast, but it did not. Figure 13 shows that the fracture network extended for the most part the entire height of the Lower Barnett Shale with some fractures extending into Ordovician-aged limestone. Considering this data and general geomechanical knowledge, the final fracture network around Pearl Cox 6 could be interpreted as a group of long hydraulic fractures extending in the southwest direction that intersect perpendicularly with natural fractures striking in the northwest direction.

4.3 DISCRETE FRACTURE NETWORK (DFN)

Having microseismic data available can be extremely beneficial. With the original data and right microseismic software, the results can be used to determine well spacing, offset well locations, refrac candidate identification, staging strategies, and real-time changes to fracture treatment design and execution in both horizontal and vertical wells. However, the only information available are the microseismic event images seen from above. Lostis (2016) used his interpretation of these images and the information in Mayerhofer et al. (2006) as a basis for interpreting his own approximation of the fracture network in the area. Lostis (2016) digitized Figure 12 and separated the data into two sets: those that have a southwest strike, which is known to be hydraulic fractures, and those that have northwest strike, which is known to be the natural fractures. Lostis (2016) then fitted a linear regression model by hand to create one realization of the discrete fracture network in the Lower Barnett Shale Formation, seen in Figure 14. This was his assumed representation of the fracture network in the Barnett Shale. Lostis (2016) only accounted for a two-dimensional representation of the fracture network.

In this research, his fracture network has been extended to 3-dimensions and was used as the DFN for the base case simulation in section 5. Since the DFN is only an interpretation of the fracture network based off of the microseismic images, five realizations of Lostis (2016) fracture network have been generated with random fracture orientations to account for little percentage of subsurface unknown. The effect of these orientations will be studied in more detail in section 6. An example of one of these realizations can be seen in Figure 15 and the rest of the realizations are in appendix A. For simplicity, the fractures have been extended the entire length of the reservoir and are considered to be homogeneous in length, permeability, and porosity.

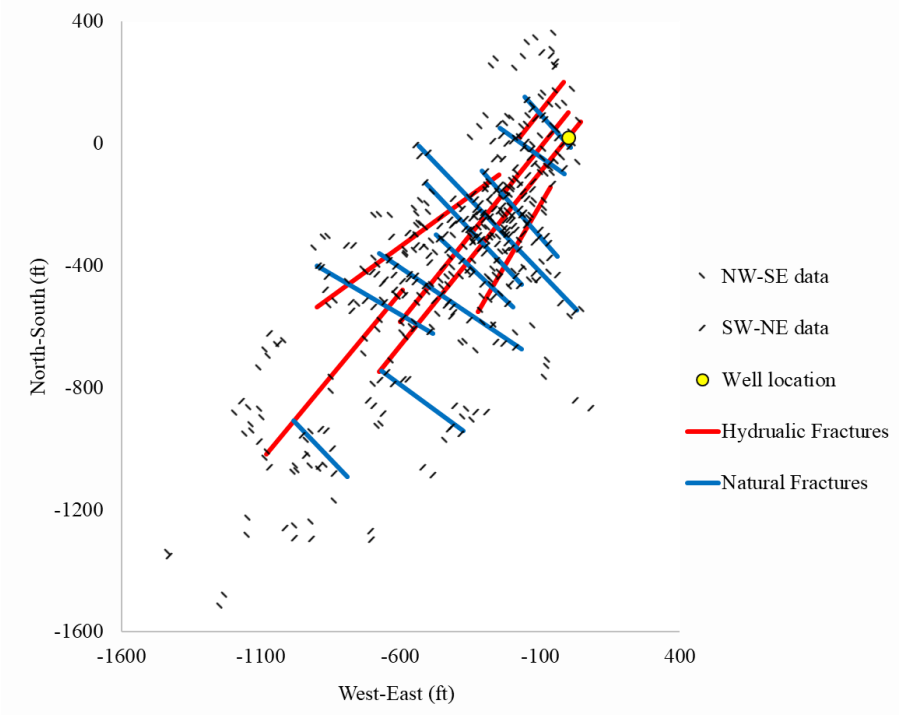

Figure 14: Base case simulation fracture network. Adopted from (Lostis, 2016). Created by linear regression. Hydraulic fractures are striking NE - SW, Natural Fractures are striking NW - SE.

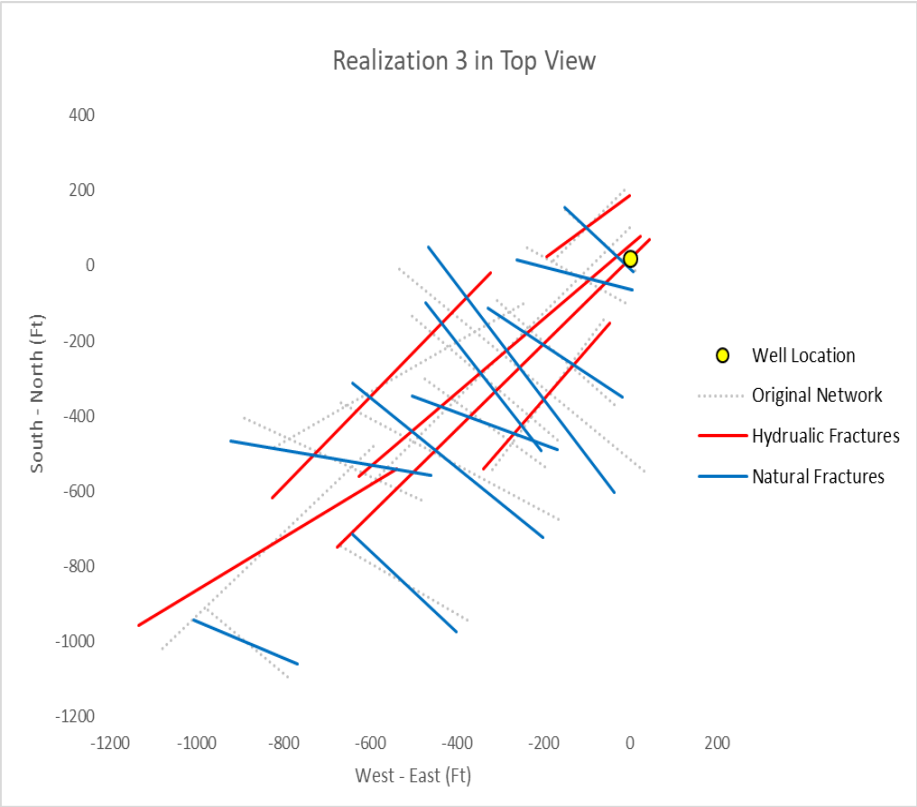

Figure 15: Example of fracture network realization in Top View.

Thus far, a brief background of the different types of modeling techniques have been reviewed, along with the principles of EDFM. This section just went over the discrete fracture networks for the simulations in this study. In the next section, the EDFM model parameters and results of the base case simulation will be discussed along with the simulation results of the multiple realizations.

5. 3D SIMULATIONS

As mentioned in the fundamentals of EDFM section, the fractures and the matrix are on separate computational domains that are coupled by NNCs to create an EDFM. The DFN used for the base case simulation was discussed in the previous section. In this section, the EDFM model parameters are examined along with the base case simulation results and model validation.

5.1 BASE CASE MODEL DESCRIPTION

Now that the Discrete Fracture Network (DFN) is built, the reservoir model needs to be created and integrated with the DFN. The pre-processing code described in section 3 integrates the reservoir model and DFN together by generating a table of transmissibility's where the NNCs are specified for each cell. The code outputs the necessary property files for the case file, which is the main file that specifies the data input files used for a simulation run in the Nexus software. For more information on the file outputs generated by the pre-processing code, please refer to section 3.

The simulator used for this research is Landmark's Nexus Reservoir Simulator. The simulation uses Nexus's GASWATER fluid system, which is used for dry gas fluid simulations. The matrix grid is 100 x 100 x 10 and the reservoir volume modeled is approximately 1400 x 1600 x 415 ft. meaning the gridblock dimensions are 14 x 16 x 41.5 ft. in the x, y, and z directions, respectively. Table 5.1 shows this information. The matrix grid and DFN are integrated by the pre-processing code making the total number of gridblocks 108,050; 100,000 matrix gridblocks and 8,050 fracture gridblocks.

Variable	Value
Grid Size (x × y × z)	100 × 100 ×10
Gridblock Dimensions (Δx(ft) × Δy(ft) × Δz(ft))	14 × 16 × 41.5
Number of Fracture Cells	8,050
Reservoir Volume Modeled	1400 (ft) × 1600 (ft) × 415 (ft)

Table 5.1: Matrix grid size and gridblock dimensions.

Table 5.2 and Table 5.3 show the model properties and well properties used for the base case 3D simulation. The parameters selected have been chosen based off of the information used in Lostis (2016) history match. It is assumed that all the fractures are vertical and the matrix properties are homogeneous. The computational time of the base case simulation was about an hour and fifteen minutes. All simulations for this study were performed using Dell Precision Tower 3420 at Texas A&M University. This 64-bit operating system, x64-based processor has an Intel® Core ™ i7-6700 CPU with a frequency of 3.4 GHz.

Reservoir Properties			
Variable	**Value**	**Variable**	**Value**
Matrix porosity (%)	6	Rock compaciton in fractures (psi^{-1})	0.000003
Matrix permeability (mD)	0.00015	Depth of GWC in fractures (ft)	7207.5
Hydraulic fracture porosity (%)	100	Capillary pressure at GWC in fractures (psi)	0.25
Hydraulic fracture permeability (mD)	150	Initial reservoir pressure (psi)	3800
Natural fracture porostiy (%)	100	Reservoir temperature (^{o}F)	180
Natural fracture permeability (mD)	30	Gas gravity	0.6
Initial gas saturaiton(%)	80	Reservoir depth (ft)	7000
Initial water saturation (%)	20	Net thickness (ft)	415

Table 5.2: Additional reservoir properties used in the simulations.

Well Properties	
Variable	**Value**
Well KH (mD-ft)	60
Wellbore radii for each completion (ft)	0.25
Effective gridblock radii for each completion (ft)	4.2962

Table 5.3: Well properties used in the simulations.

A hydraulics table that simulates a tubing string has been implemented into the model as well because the wellhead pressure is trying to be matched. A copy of the hydraulics table can be found in appendix C. The production history used came from Devon Energy and was of the well behavior of well Pearl Cox 6 over approximately 7 years, between 2001 and 2008. The surface gas rates in model have been constrained to match the production history, while the surface water rates and tubing head pressure are unconstrained. The well has been completed the entire height of the reservoir.

5.2 BASE CASE SIMULATION RESULTS

The reservoir properties used in Table 5.2 and 5.3 were used to run a 3D simulation of well Pearl Cox 6 in the Barnett Shale. The well was constrained in terms of surface gas rate using the field production history data. The results of the base simulation can be seen in Figures 16 - 19. Figure 16 shows the data results of the surface gas rates of the base simulation compared to the historical behavior. Since surface gas rate constraints were added to the model, the gas rate pretty much fits the historical data exact. Figure 17 shows the data results of the surface water rates of the base simulation compared to the historical behavior. The historical water rate is very sporadic with days of high rates followed by days with low rates. Due to this sporadic water rate data, trying to match the historical data proved to be very difficult because the base simulation water rate curve decreases at

a much smoother rate. Nevertheless, the water rate follows the general trend of the historical field behavior. Figure 18 shows the data results of the wellhead pressure (tubing pressure) of the base simulation compared to the historical behavior. The pressure drop experienced by the well was impacted by the gas rate constraints. The wellhead pressure of the base case simulation fits the production history fairly well and can be argued that it is a reasonable agreement between the simulated and observed historical field behavior. Figure 5.4 shows the cumulative gas production of the simulation at a total of 1107 MMSCF. This fit the production history well, but we only have cumulative production history up to April 2005. The results were very similar to Lostis (2016) 2D history match simulation. This is expected since his model influenced the properties used and the discrete fracture network orientations were influenced from his model.

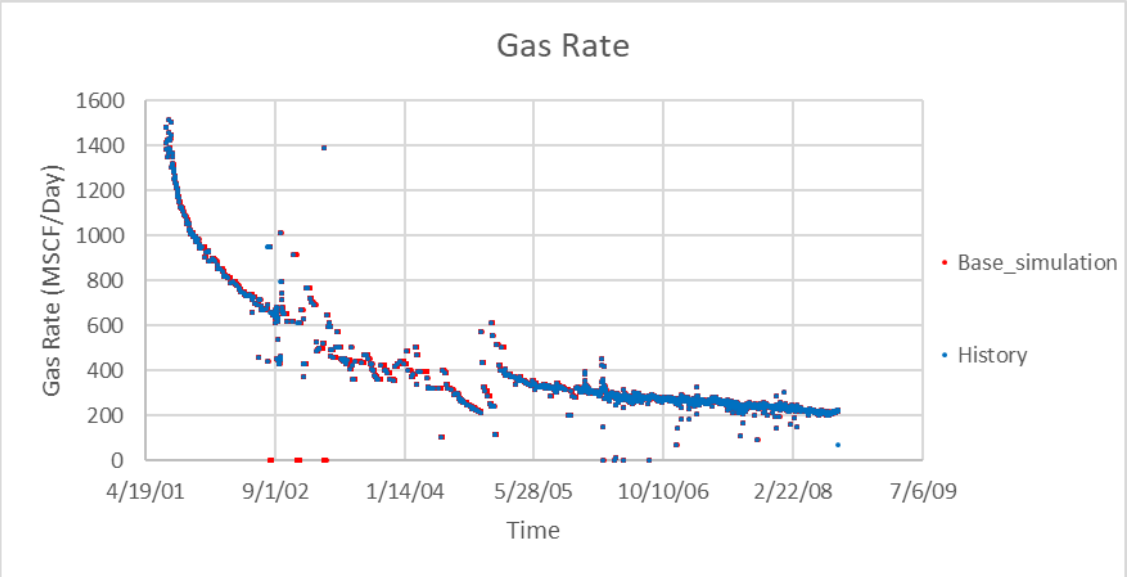

Figure 16: Surface Gas rates of base case simulation versus historical data.

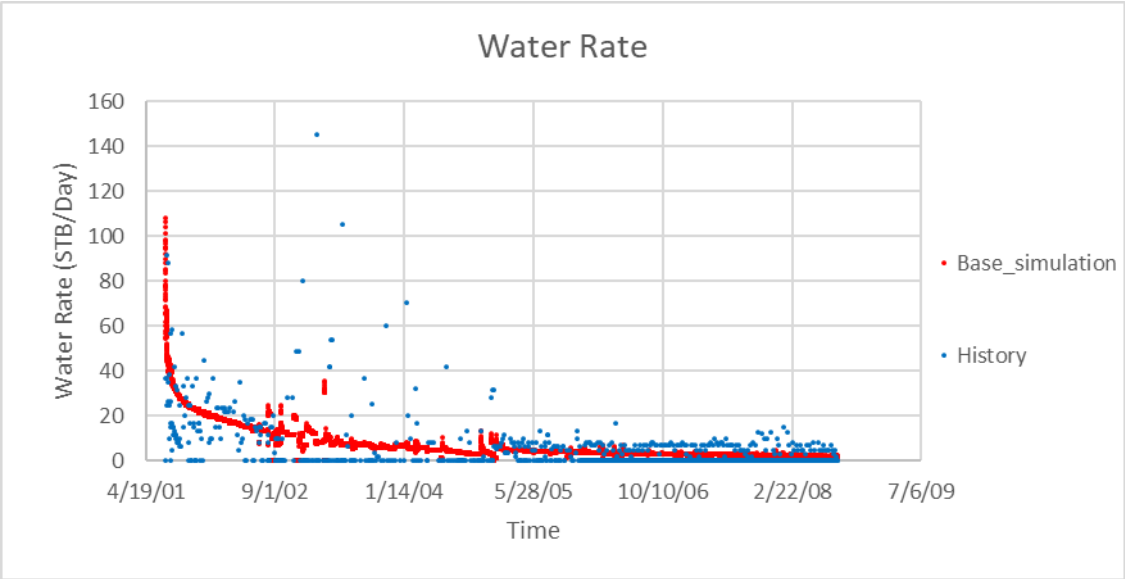

Figure 17: Surface water rates of base case simulation versus historical data.

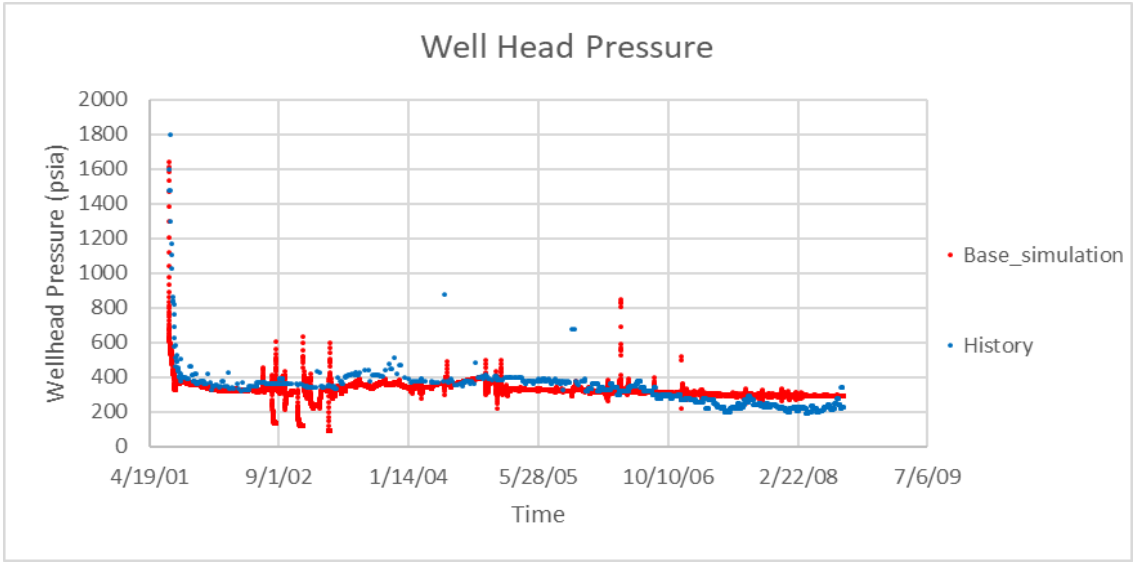

Figure 18: Wellhead pressure of base case simulation versus historical data.

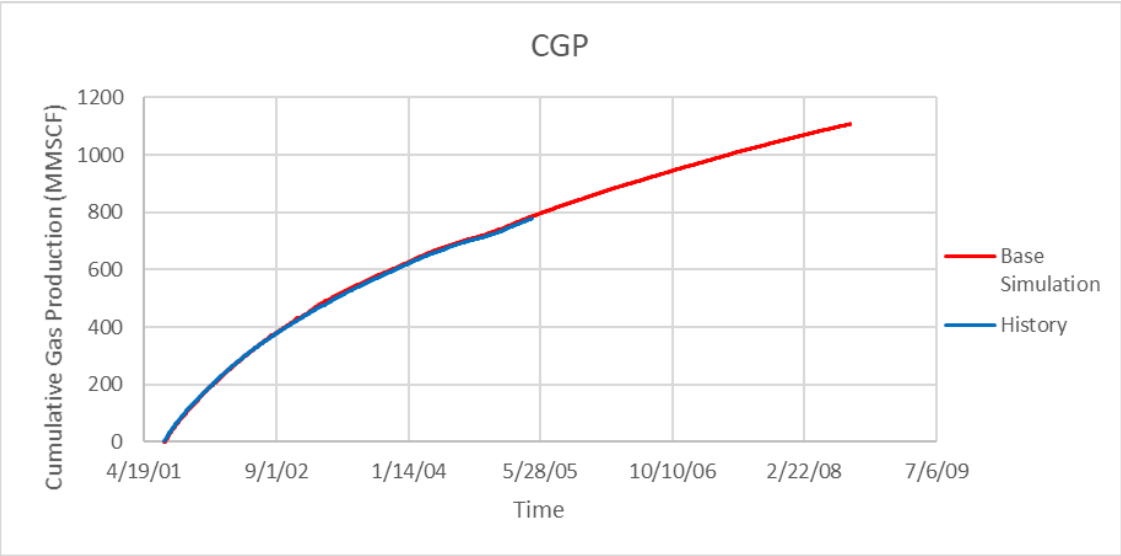

Figure 19: Cumulative Gas Production of base case simulation versus historical data.

5.3 DIFFERENT REALIZATION SIMULATION RESULTS

As seen in Figure 18, the wellhead pressure relatively fits the field history behavior. However, since multiple realizations of the fracture network have been generated to account for uncertainty, the simulation was repeated with the other five fracture network realizations to see if the different fracture orientations could better fit the historical wellhead pressure. Since there are constraints on the surface gas rate, it is predicted that the gas rate should not change from the base case simulation. The results expected to change are the wellhead pressure and the water rate. The model parameters used for these simulations are the same as table 5.2 and 5.3. Also in these simulations, one hydraulic fracture was left connected to the well, due to a study done by Li and Lee (2008). In this paper, the authors conducted different numerical examples of the fracture network in the reservoir. They concluded that the intersection of fracture with the production well

significantly enhances the well productivity. So, based on this assumption, if no fractures are in contact with the production well the productivity will decrease significantly. The different fracture network realizations can be found in appendix A.

After running the simulations, it was found that realization 2 actually fits the wellhead pressure better than the base case simulation. From this, it can be argued that this fracture network realization is a better representation of the actual fracture network in the reservoir. Results of each simulation can be found in appendix B.

5.4 MODEL VALIDATION

The whole point of a model validation or history match is to achieve a reasonable agreement between the simulated and the observed historical field behavior. It can be argued that this reasonable agreement was reached with the base case. However, running the different fracture realization simulations, it is seen in Figure 22 that realization 2, found in appendix A, matched the wellhead pressure better than the base case simulation. Figures 20 and 21 show the gas rate and water rates were about the same. So, Realization 2 will be considered our history matched model. Although the wellhead pressure fit better than the base case simulation, the cumulative gas production was increased slightly compared to the base case with a total of 1117 MMSCF. This resulted in the cumulative gas production to produce more than the field history. This was most likely caused by the connectivity of the fracture network, allowing more fluid to flow between the fractures. With these results, it can be said that the model is validated.

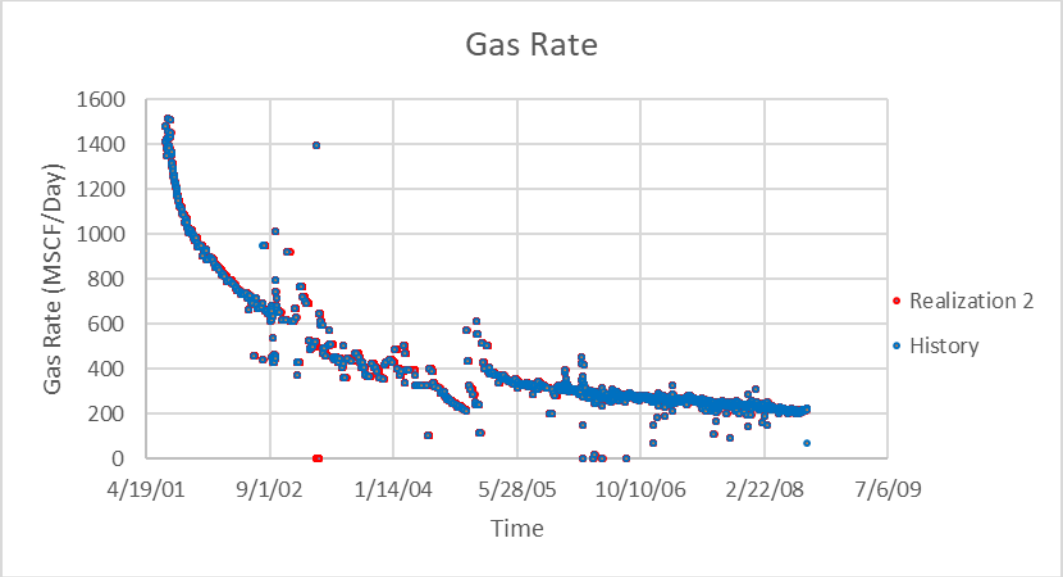

Figure 20: Surface gas rate of realization 2 versus historical data.

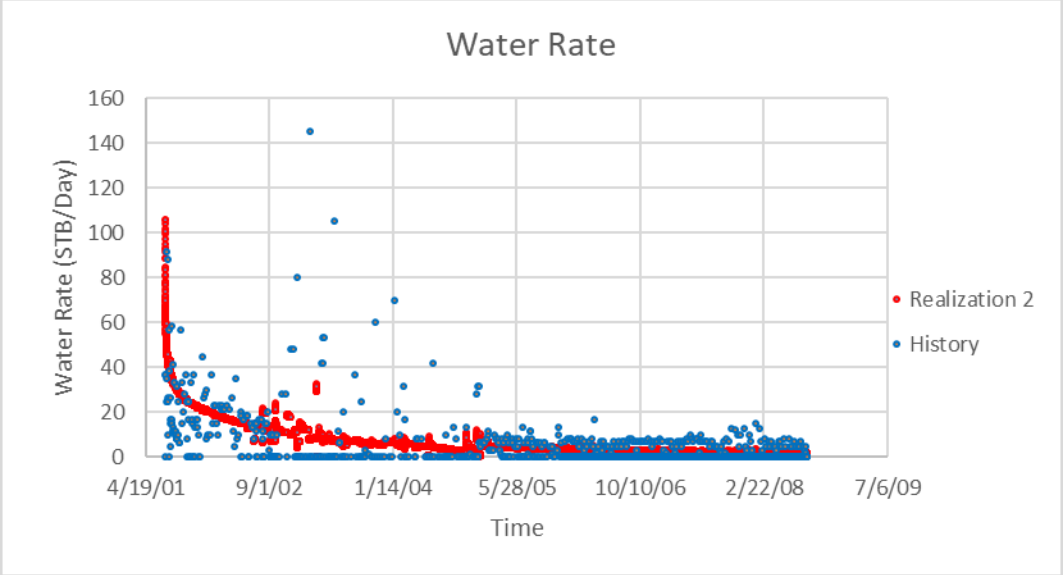

Figure 21: Surface water rate of realization 2 versus historical data.

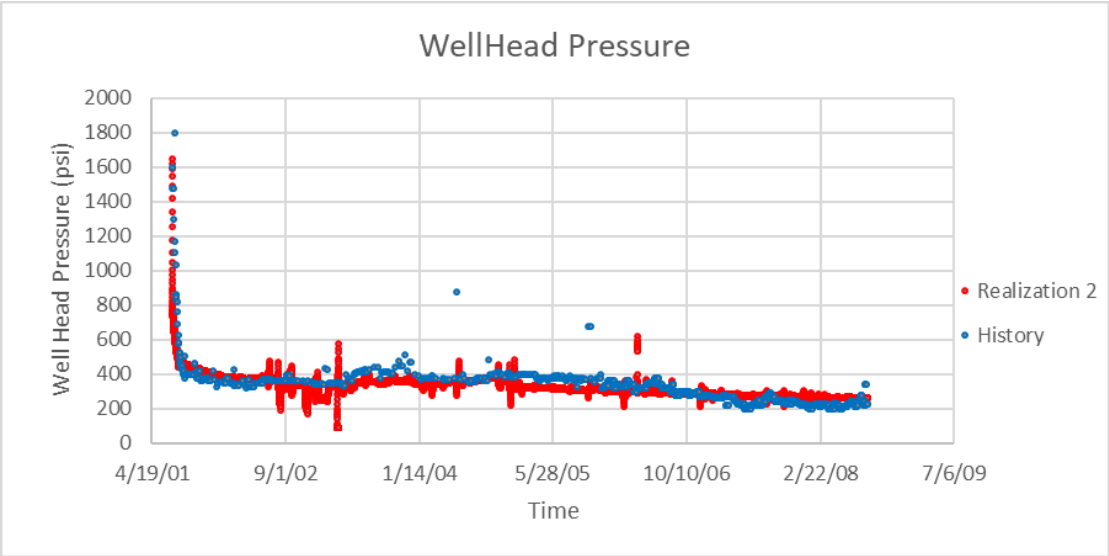

Figure 22: Wellhead pressure of realization 2 versus historical data.

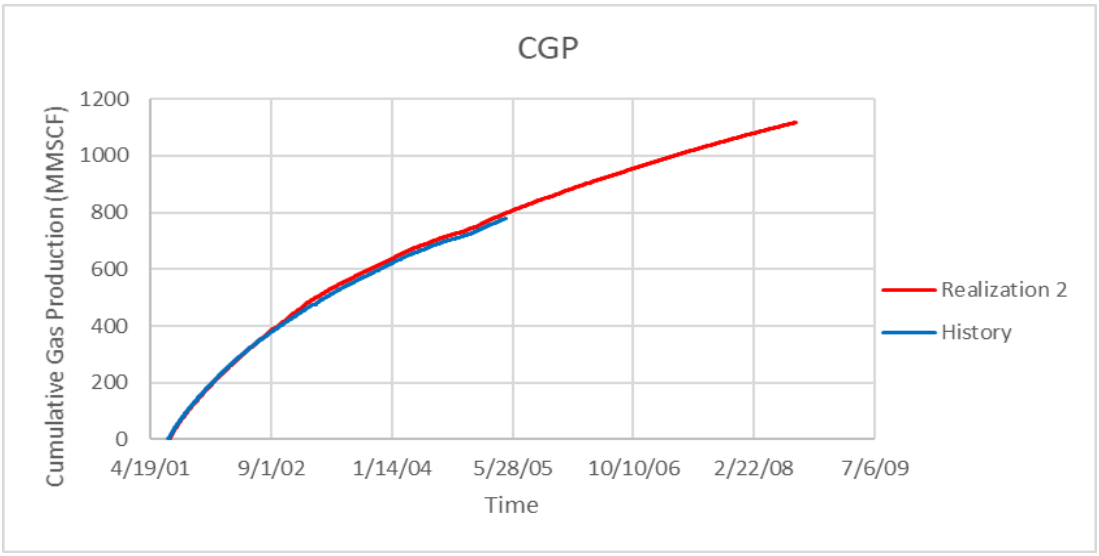

Figure 23: Cumulative Gas Production of realization 2 versus historical data.

5.5 VISUALIZING RESERVOIR DEPLETION

In order to visualize what is happening at different layers within the reservoir, we created a script to produce top-view profile maps of pressure and gas saturation. This script

structures the Nexus cell arrays which were originally unstructured to produces profile maps that show the matrix gridblocks at each layer.

It can be seen in Figure 24 that the pressure drawdown imposed at the well spreads throughout the fracture network rapidly within a few days and layers. The depleted region increases with time. At the end of year one, the areas around the fracture network are depleted. The matrix regions that have not been reached by the fracture network are not depleted and this is due to the low permeability matrix (100 mD). Going down by layer, layer 10 has a larger pressure drawdown than layer 1; this is due to production starting at the bottom of the well. Note that we are visualizing the pressure, and gas saturation in the matrix gridblocks only, not in the fracture gridblocks where the fluid saturation and relative permeability behavior are different. Before the start of production, all of the matrix gridblocks are initialized at the connate water saturation which is 0.20. In Figure 25, the gas saturation profile is shown. As gas from the matrix gridblocks flow to the fractures, the gas saturation in those cells decrease. We are inferring from the figures that there is greater water with depth.

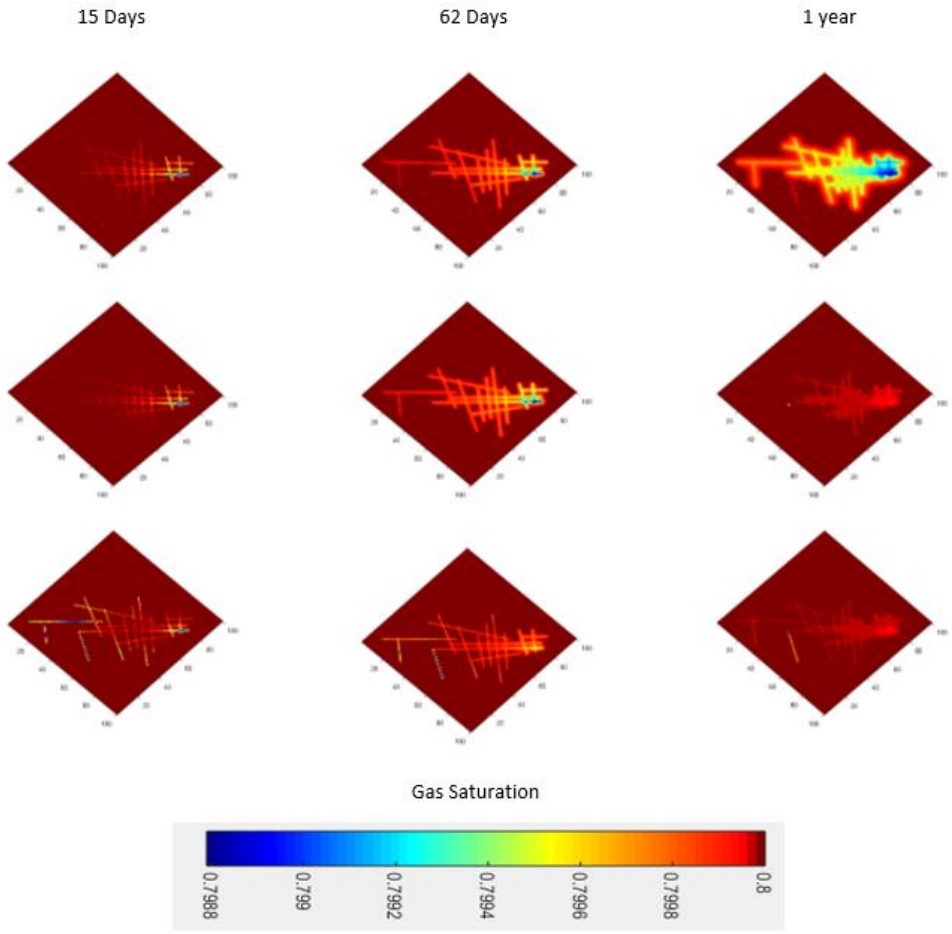

Figure 24: Pressure Profile of layer 1, 5, and 10, respectively going down at 15 days, 62 days, and 1 year, respectively.

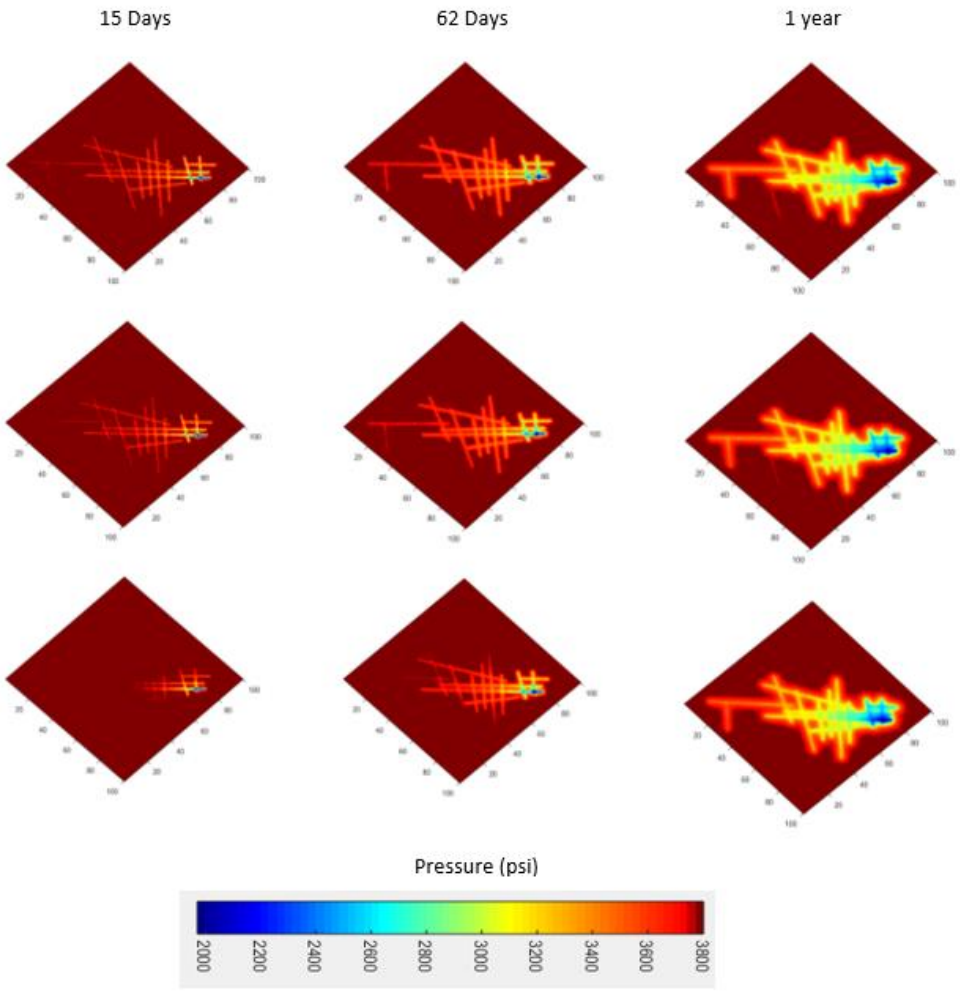

Figure 25: Gas saturation profile of layer 1,5, and 10, respectively at timesteps 15 days, 62 days, 1 year.

6. VERTICAL WELL PARAMETRIC STUDY

The following parametric study for vertical wells is presented to show how fracture network orientation and density affect vertical well productivity. Due to slight differences in wellhead pressure of the different fracture realization simulations of section 5, we need to see the actual impact that each realization had on productivity. The first part will discuss the effect that each realization had on production. The second part will discuss the impact that fracture density (fracture spacing) has on productivity.

6.1 IMPACT OF FRACTURE ORIENTATION

To see the full influence of the change in fracture orientation, we changed the surface network and run control parameters of our 3D model. In our previous simulations, we set surface gas constraints to be able to match the production history behavior. In the parametric study, the run control is set to run implicitly and we have used a correlation instead of the hydraulics table for tubing head pressure. This has decreased the run time of simulation from an hour and fifteen minutes to about 15 minutes. We have set one constant gas flow rate for the whole simulation set at the maximum historical rate of 1500 MSCF and set a minimum wellhead pressure for the wellhead connection to 100 psi. This will give varying rates for each well to see the full impact of each random realization. Other than the surface network properties and run control parameters, the rest of the model parameters are the same from Table 5.2 and 5.3.

Figure 26 and Figure 27 show the cumulative gas production and cumulative water production simulation results, respectively. For both of these figures, the fracture realization that significantly increased production was realization 4. From the top view

map of realization 4, seen in appendix A, it can be seen that this realization has high fracture connectivity in the middle of the network, meaning the fracture to fracture intersection is very high. This allows for more fluid to flow between the fractures, causing there to be higher production of gas and water. Also, there are multiple fractures intersecting with the well allowing more fluid to reach the well. It can also be seen that the two realizations that have multiple fractures near the well location tend to have better well performance. The fracture realization that significantly decreased productivity was realization 5. From the top view map of realization 5, seen in appendix A, it can be seen that this realization has less fracture connectivity compared to the other realizations.

In conclusion to this section, correlations show that fracture networks that have more connectivity and more fracture-well intersection result in better well performance. This fracture network connectivity depends on the orientation of the fractures. Although there is no historical data at the surface rates we have imposed, if given historical data, it can be argued that this method could be an effective way to indicate the actual fracture orientation of the reservoir.

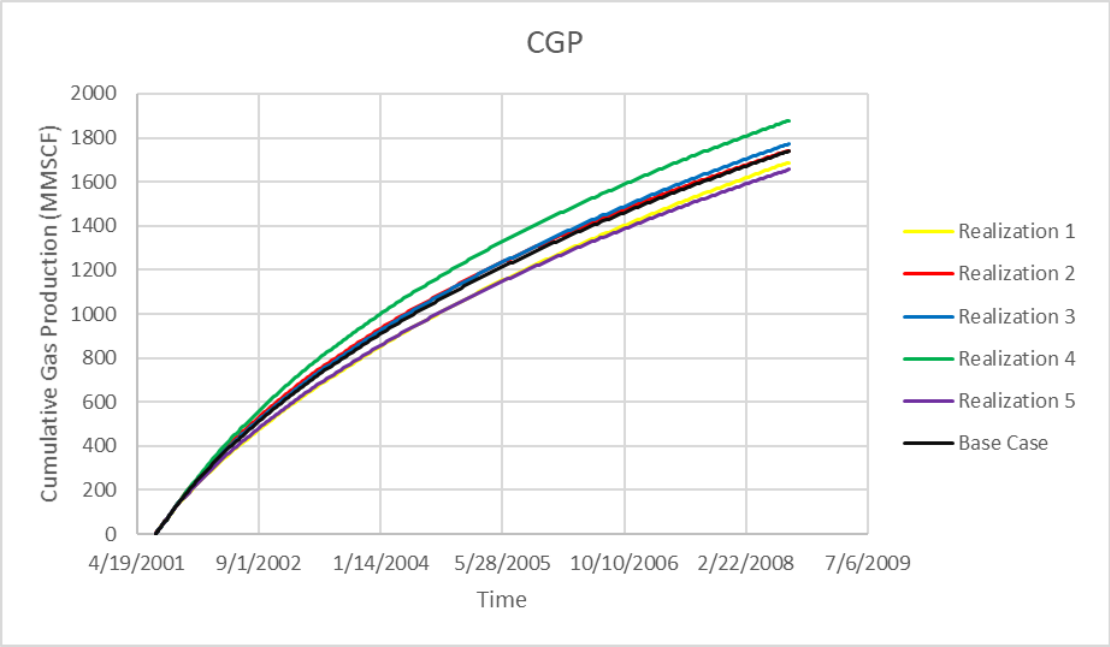

Figure 26: Cumulative Gas Production with constant surface gas rate of 1500 MSCF of different fracture orientations.

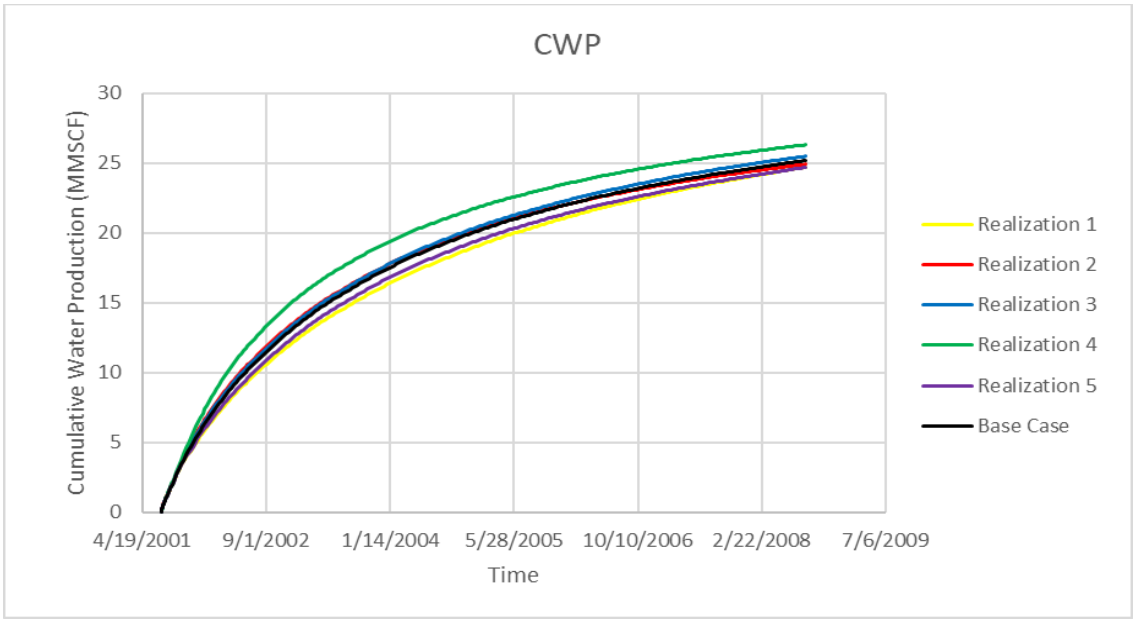

Figure 27: Cumulative Water Production with constant surface gas rate of 1500 MSCF of different fracture orientations.

6.2 IMPACT OF FRACTURE DENSITY

Fracture orientation can play a crucial role in the productivity of a well. The orientations play a significant role in the connectivity of the network as a whole and as we learned in section 6.1, fracture networks with high connectivity have a better result in well performance. Another parametric study has been conducted on the impact of fracture density. In previous studies like Mayerhofer 2005, it was seen that higher fracture densities have better production results. We have tested this using EDFM.

Figure 28 and 29 are top view maps of the fracture density in the reservoir. Figure 28 shows a fracture network with half of the fracture density compared to our base case simulation fracture network. Figure 29 shows the fracture density doubled.

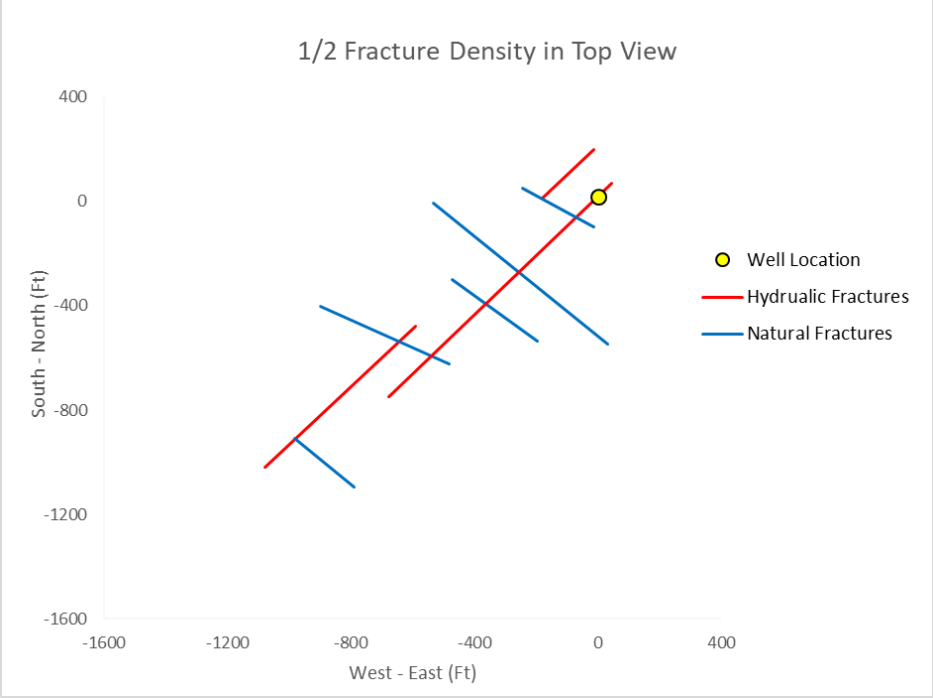

Figure 28: Top view map of 1/2 fracture density.

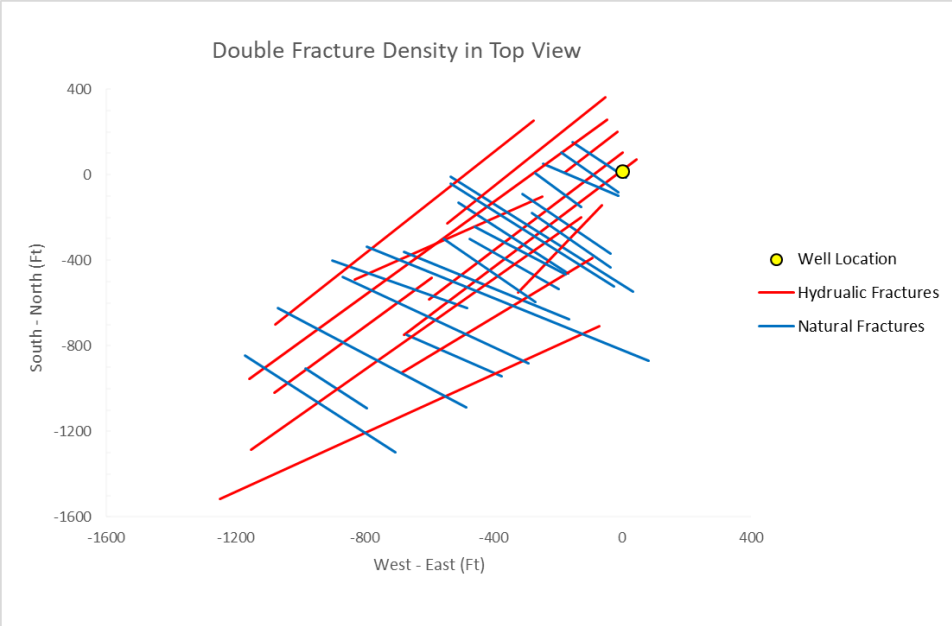

Figure 29: Top view of fracture network with double fracture density.

Figures 30 and 31 show the results of the simulation. For this study, the parameters used were the same as section 6.1. The surface rates were imposed at a constant rate of 1500 MSCF and a 100-psi minimum wellhead pressure. The model variables were the same as table 5.2 and 5.3. It can be clearly seen that the higher the fracture density, meaning smaller spacing between the fractures, the better well performance. This is in line with previous studies done on fracture density. I also ran this simulation completing the well only 5 layers and not the full extent of the reservoir. With this simulation, it showed only completing the well half way produced less fluids than completing the full reservoir.

To conclude for the impact of fracture density, the larger the fracture density, the better the well performance. This means that the smaller the spacing between each fracture, the more productivity.

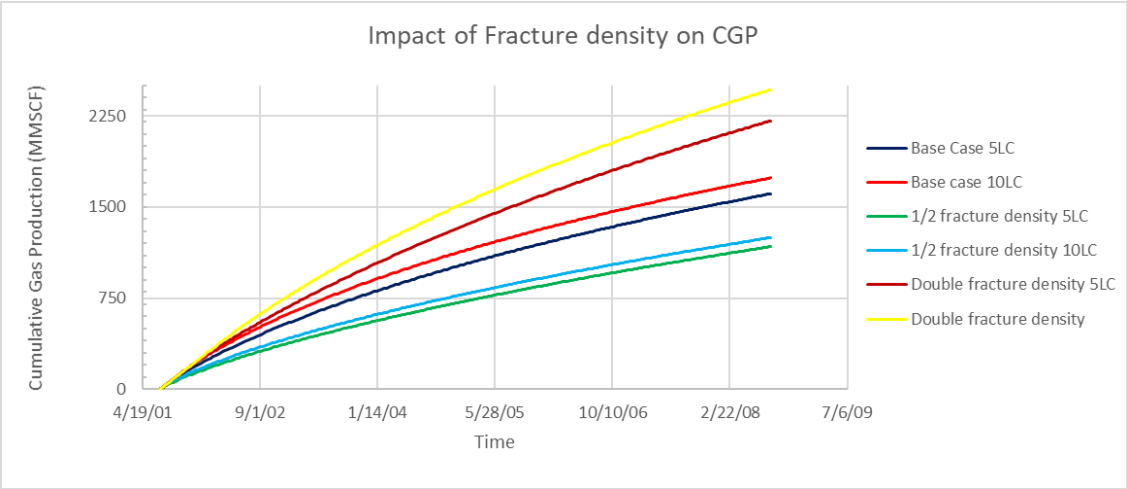

Figure 30: Impact of fracture density on Cumulative gas production. 5LC means 5 layer completions. 10LC means 10 layer completions.

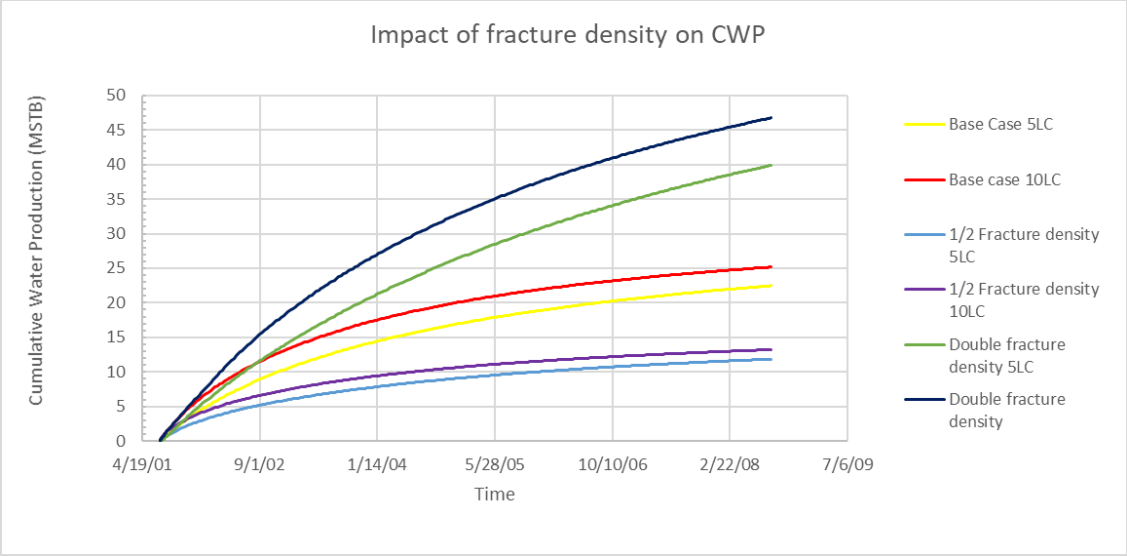

Figure 31: Impact of fracture density on Cumulative water production. 5LC means 5 layer completions. 10LC means 10 layer completions.

7. CONCLUSIONS AND RECOMMENDATIONS

7.1 CONCLUSIONS

In this study, an EDFM was built in 3D to simulate and match well Pearl Cox 6, a hydraulically fractured vertical well in the Barnett Shale. The base case simulation proved to match the production history fairly well, but to account for fracture network uncertainty, multiple fracture network realizations were created and simulated. It was seen that realization 2 fit the historical wellhead pressure better than the base case simulation, validating the model and possibly predicting the actual orientation of the fracture network in the subsurface.

Two parametric studies were conducted to see the impact of fracture orientation and fracture density. In the fracture orientation study, it was concluded that the orientation of the fractures played an important role when the orientation caused high connectivity between the fractures. The higher the connectivity, the better the well performance. In the fracture density study, it was concluded that the higher the fracture density, the better well performance. This is predictable since higher density allows more fluid flow to the well.

In conclusion to this study, the EDFM approach proved to be a reliable resource for field scale reservoir simulation. The computational time was reasonable at an hour and fifteen minutes and produced results that fit history fairly well.

7.2 RECOMMENDATIONS FOR FUTURE

Recommendations for future studies include conducting the same workflow for a horizontal well in different field scale reservoir, incorporate all physics that have

considerable impact on fluid flow into the hybrid model to develop a complete and robust unconventional simulator, and studying the impact of a more heterogeneous fracture network with different lengths, widths, and orientations.

REFERENCES

Breyer, J.A., 2012, Shale Reservoirs, in J.A. Breyer, ed., Shale reservoirs-Giant resources for the 21st Century: AAPG Memoir 97, p. x-xii.

Farid, S. M. 2015. Modeling Shale Gas Flow Using the Idea of Apparent Dynamic Permeability. Master of Science Thesis, Texas A&M University.

Fisher, M. K., Wright C. A., Davidson B. M., et al. 2005. Integrating Fracture-Mapping Technologies To Improve Stimulations in the Barnett Shale. SPE Production & Facilities,20(02):85–93.

Karimi-Fard, M., Durlofsky, L.J., and Aziz, K., 2004, An efficient discrete-fracture model applicable for general purpose reservoir simulators, SPE Journal, Vol. 9, 227-236.

Li, L. and Lee, S. H. 2008. Efficient Field-Scale Simulation of Black Oil in a Naturally Fractured Reservoir through Discrete Fracture Networks and Homogenized Media. SPE Reservoir Evaluation and Engineering, 11(04).

Lostis, G. 2016. Using the Embedded Discrete Fracture Model to Match the Production History of a Hydraulically-Fractured Shale Gas Well. Master of Engineering Thesis, Texas A&M University.

Mayerhofer, M. J., Lolon E. P., Youngblood J. E., and Heinze J. R. 2006. Integration of Microseismic Fracture Mapping Results With Numerical Fracture Network Production Modeling in the Barnett Shale. Presented at the SPE Annual Technical Conference and exhibition in San Antonio, Texas, USA, 24-27th September.

Moinfar, A. 2013. Development of an Efficient Embedded Discrete Fracture Model for 3DCompositional Reservoir Simulation in Fractured Reservoirs. PhD Dissertation, The University of Texas at Austin.

Moinfar, A., Abdoljalil V., Sepehrnoori K., and Johns R. T. 2014. Development of an Efficient Embedded Discrete Fracture Model for 3D Compositional Reservoir Simulation in Fractured Reservoirs. SPE Journal, 19(02)

Pollastro, R.M., Jarvie D.M., Hill R.J., Adams C.W., 2007. Geologic framework of the Mississippian Barnett Shale, Barnett-Paleozoic total petroleum system, Bend-arch-Fort Worth Basin, Texas. AAPG Bulletin, V. 91, No. 4, pp. 405-436.

Satter, A., Iqbal, G.M. 2015. Reservoir Engineering: The Fundamentals, Simulation, and Management of Conventional and Unconventional Recoveries, Gulf Professional Publishing, Pg. 488

Scott et al. 2005. Mississippian Barnett shale, Fort Worth Basin, North Central Texas: gas shale play with multi-trillion cubic foot potential.

Shakiba, M. 2014. Modeling and Simulation of Fluid Flow in Naturally and Hydraulically Fractured Reservoirs Using Embedded Discrete Fracture Model (EDFM). Masters Thesis, The University of Texas at Austin.

U.S. Energy Information Administration. 2017. Annual Energy Outlook 2017.

Williams-Stroud, S. 2008. Using Microseismic Events to Constrain Fracture Network Models and Implications for Generating Fracture Flow Properties for Reservoir Simulation. Presented at the SPE Shale Gas Production Conference in Fort Worth, Texas, USA,16-18th November.

Xu, Y. 2015. Implementation and Application of the Embedded Discrete Fracture Model (EDFM) for Reservoir Simulatinon in Fractured Reservoirs. Masters Thesis, The University of Texas at Austin.

Yalcin, E. 2015. Nano-Scale Considerations for Shale Gas Flow Simulation. Master of Science Thesis, Texas A&M University.

APPENDIX

A: Fracture Realizations

Figure 32: Realization 1 in Top view.

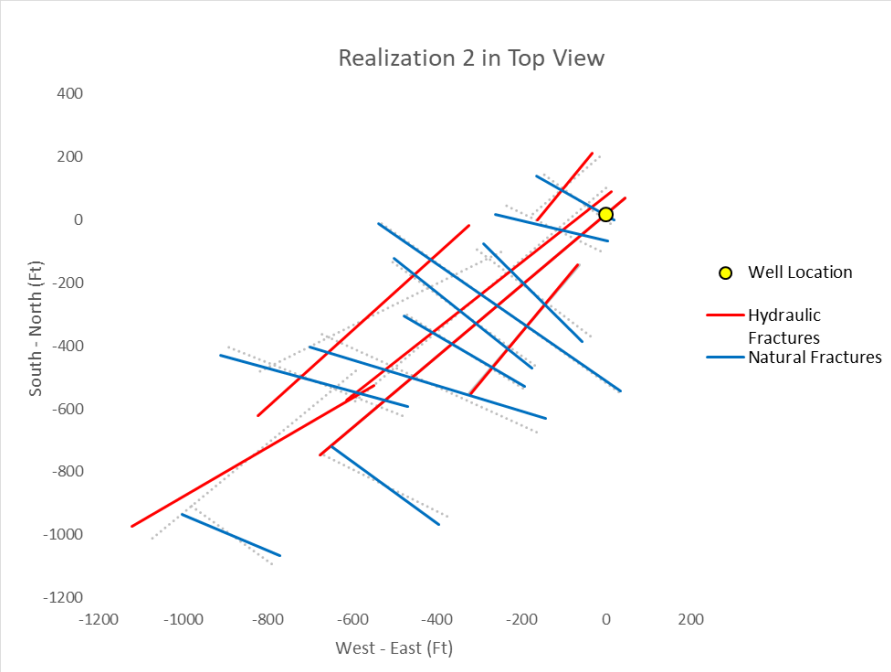

Figure 33: Realization 2 in top view.

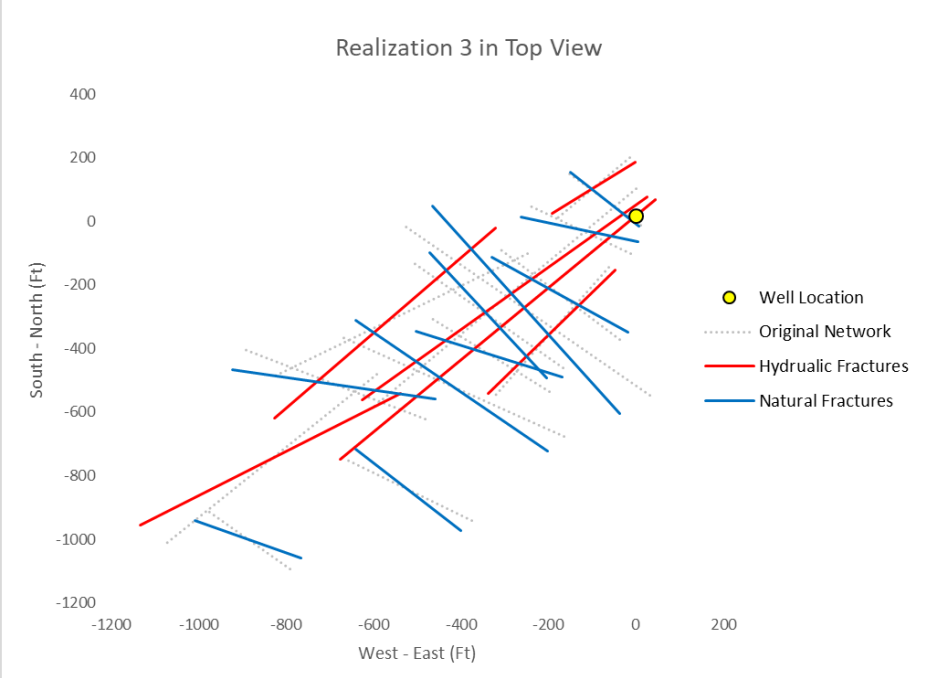

Figure 34: Realization 3 in top view.

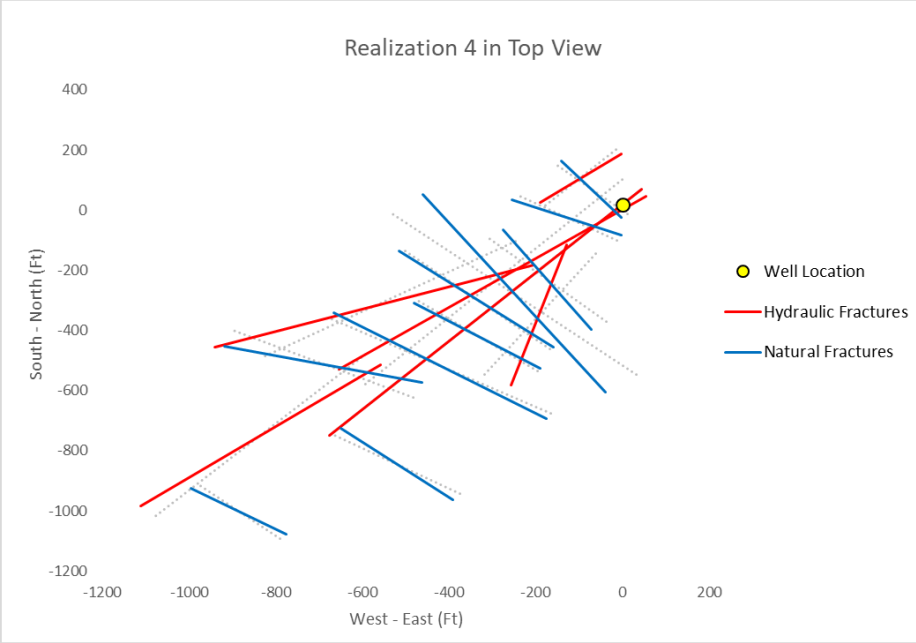

Figure 35: Realization 4 in top view.

Figure 36: Realization 5 in top view.

B: Fracture Realization Simulation Results

Realization 1

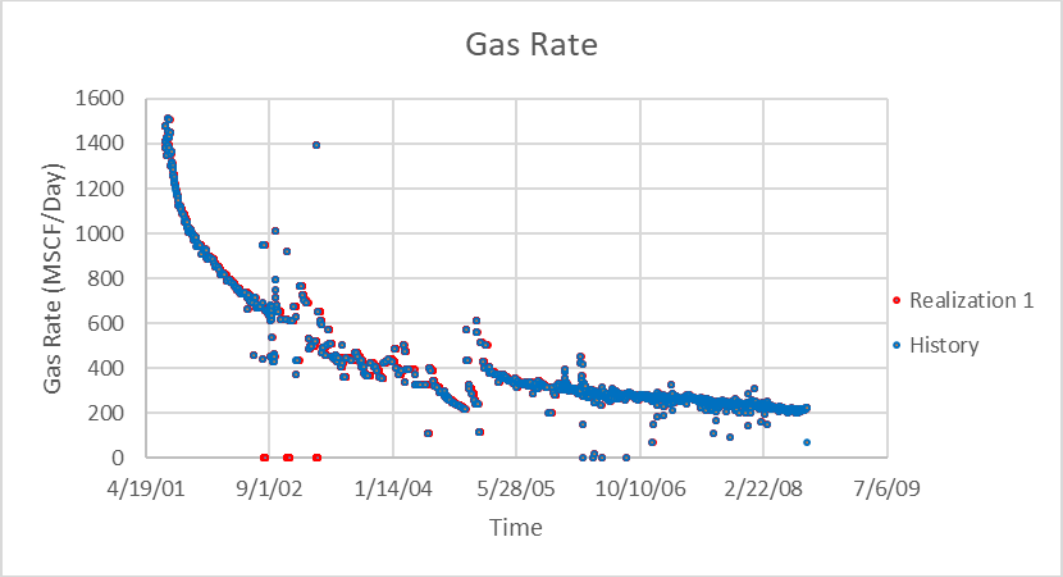

Figure 37: Gas rate of realization 1 versus production history.

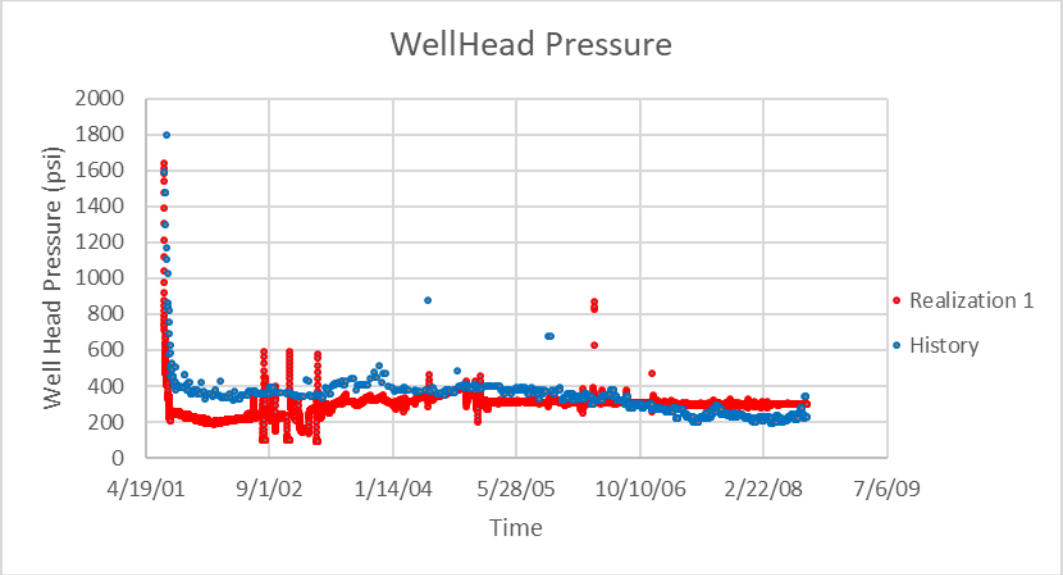

Figure 38: Wellhead pressure of realization 1 versus production history.

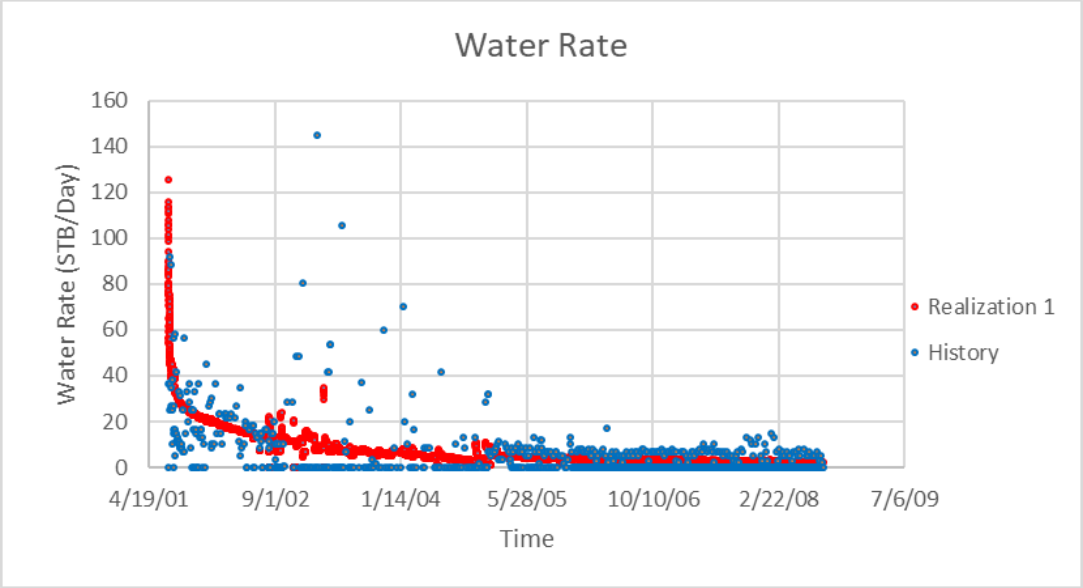

Figure 39: Water rate of realization 1 versus production history.

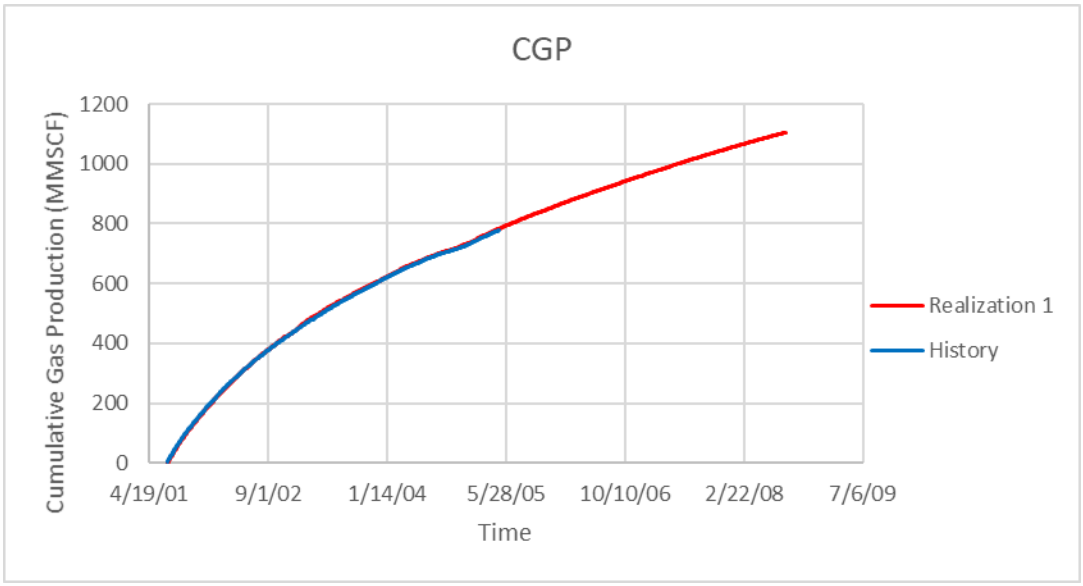

Figure 40: Cumulative gas production of realization 1 versus production history.

Realization 2

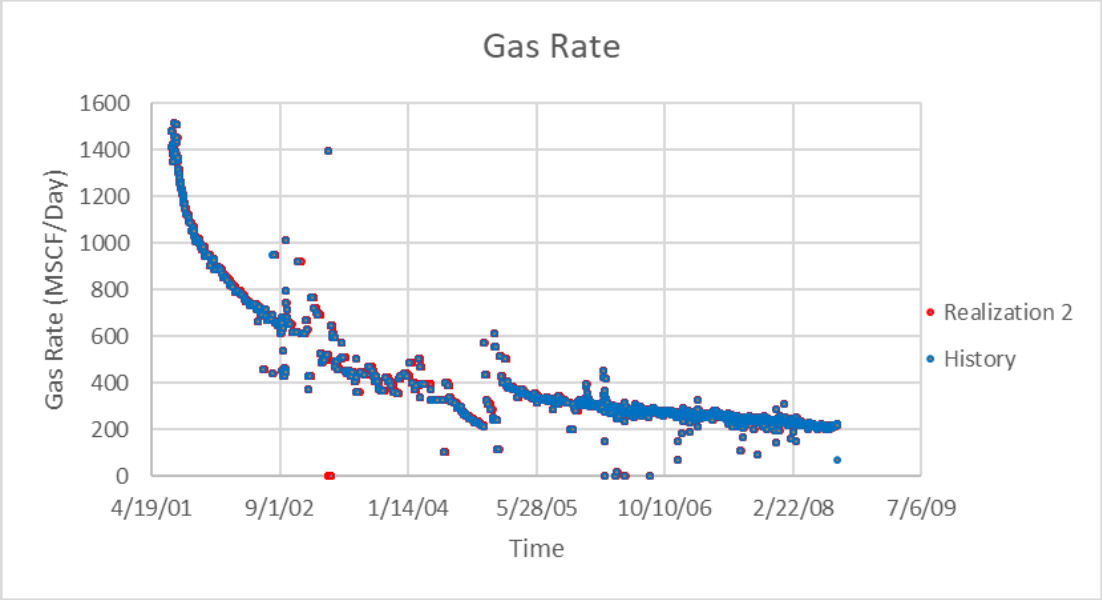

Figure 41: Gas rate of realization 2 versus production history.

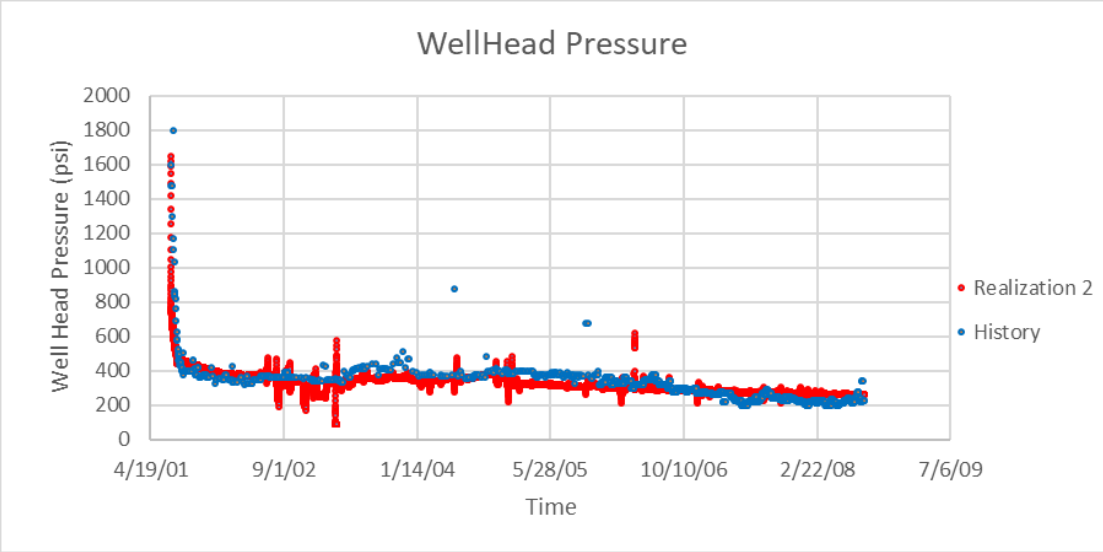

Figure 42: Wellhead pressure of realization 2 versus production history.

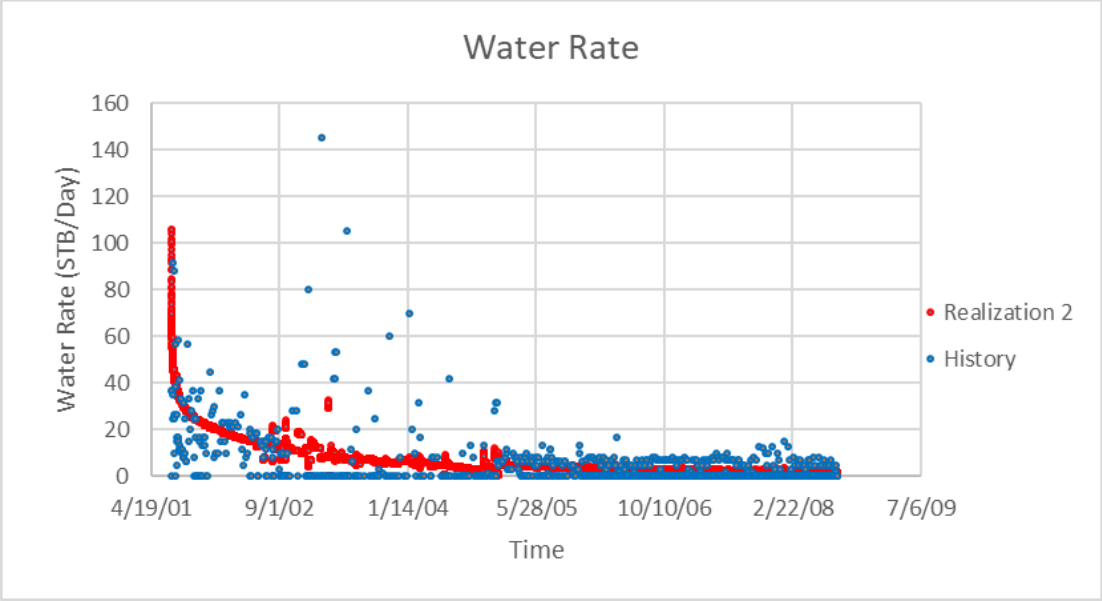

Figure 43: Water rate of realization 2 versus production history.

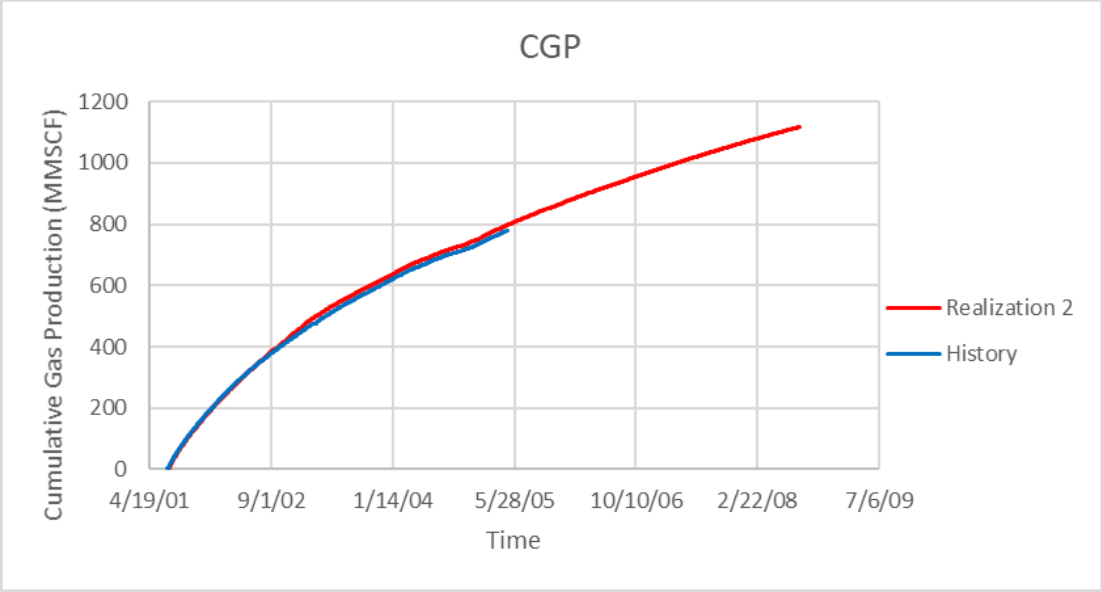

Figure 44: Cumulative gas production of realization 2 versus production history.

Realization 3

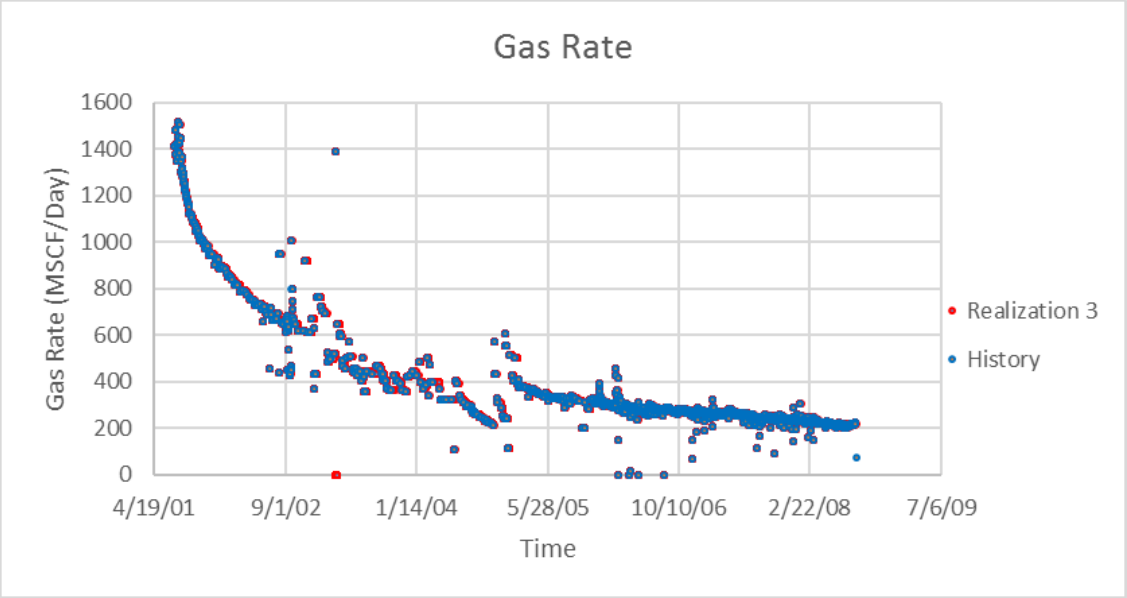

Figure 45: Gas rate of realization 3 versus production history.

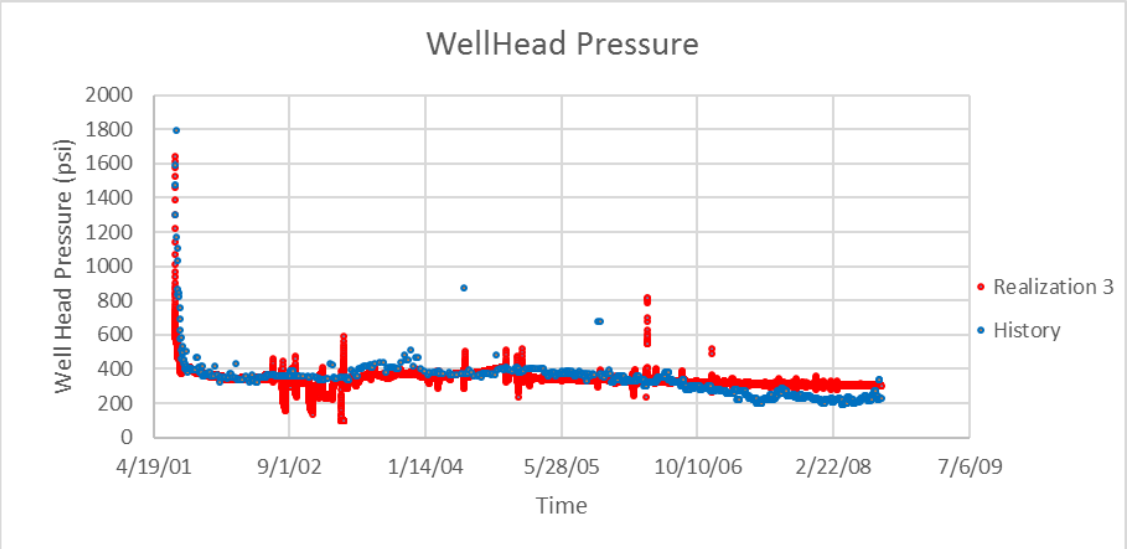

Figure 46: Wellhead pressure of realization 3 versus production history.

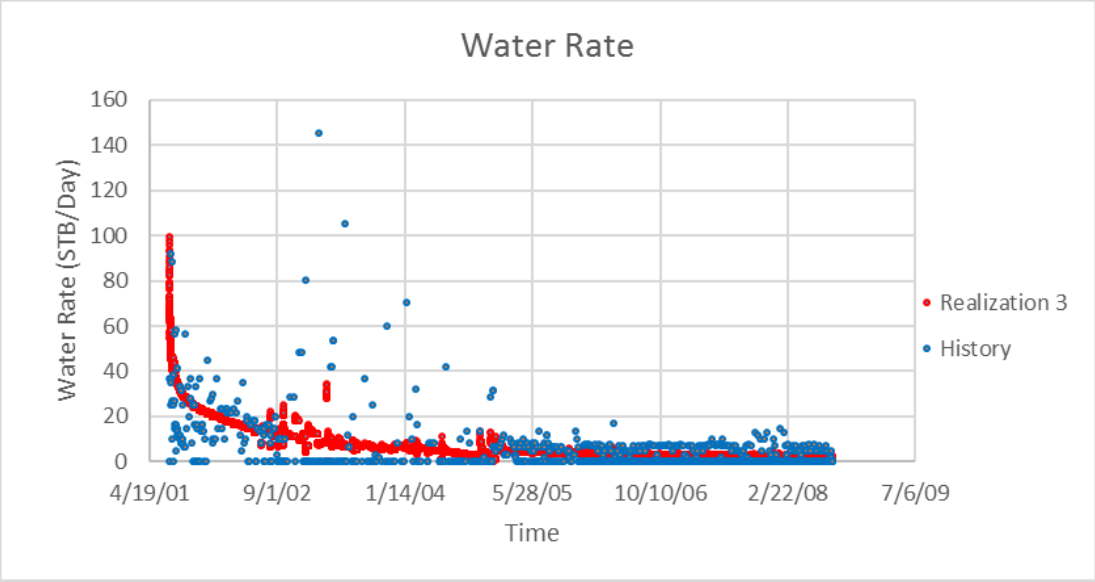

Figure 47: Water rate of realization 3 versus production history.

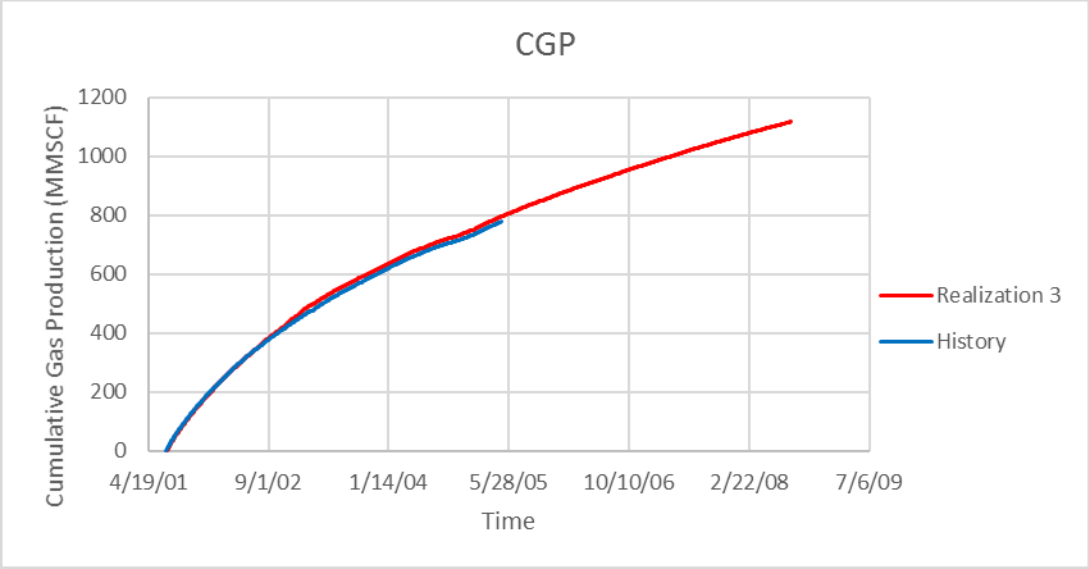

Figure 48: Cumulative gas production of realization 3 versus production history.

Realization 4

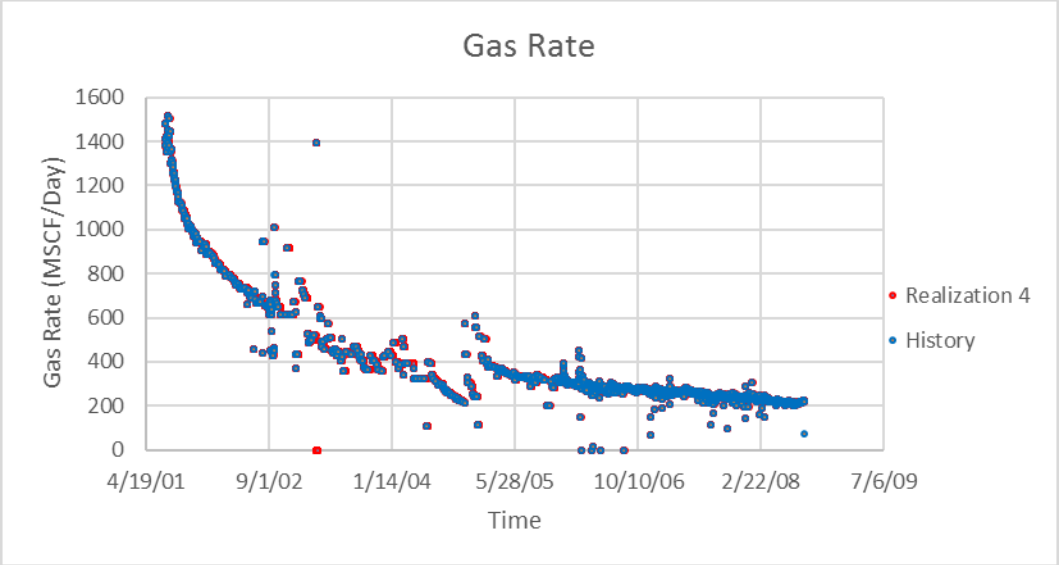

Figure 49: Gas rate of realization 4 versus production history.

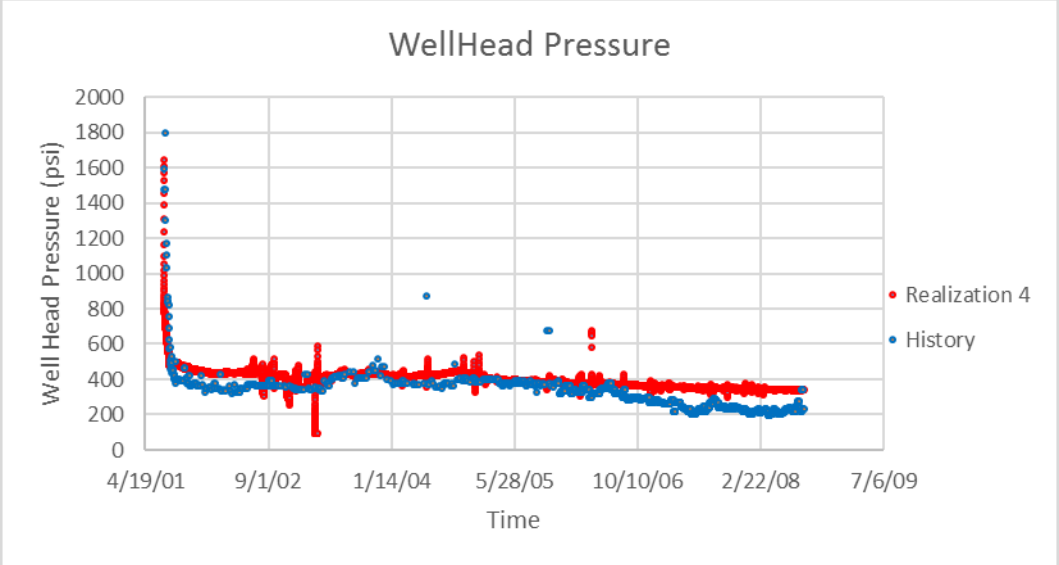

Figure 50: Wellhead pressure of realization 4 versus production history.

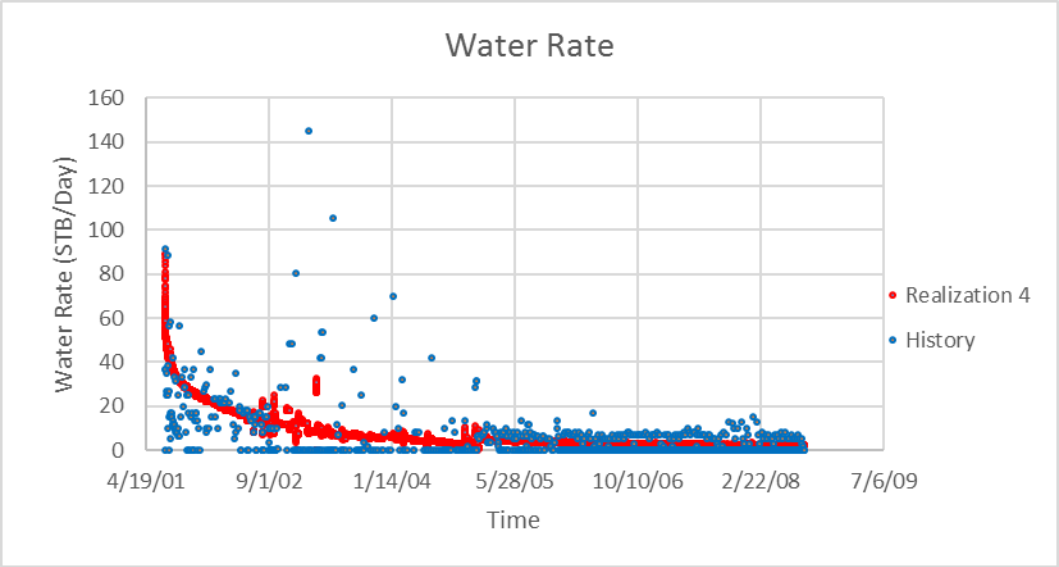

Figure 51: Water rate of realization 4 versus production history.

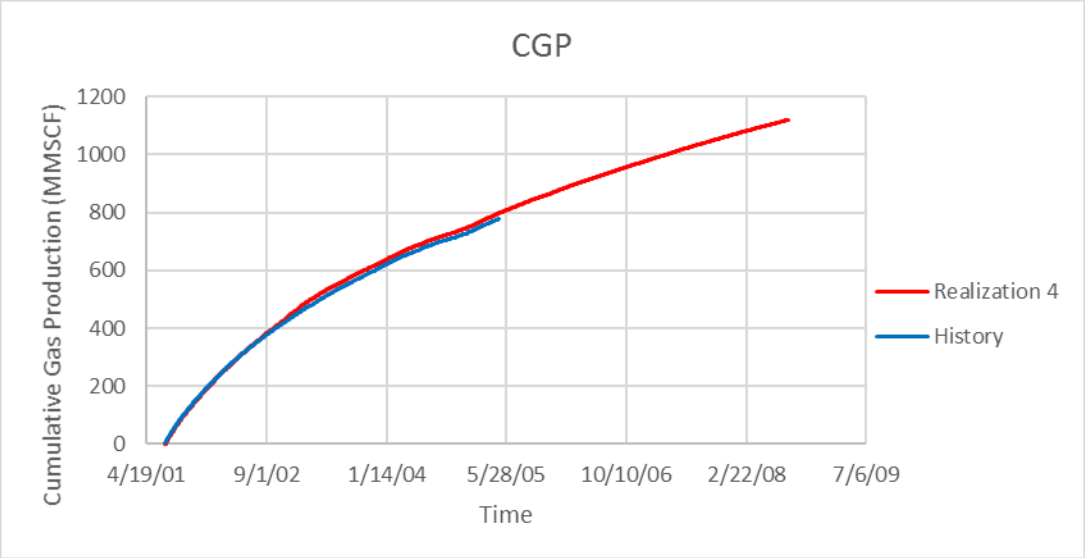

Figure 52: Cumulative gas production of realization 4 versus production history.

Realization 5

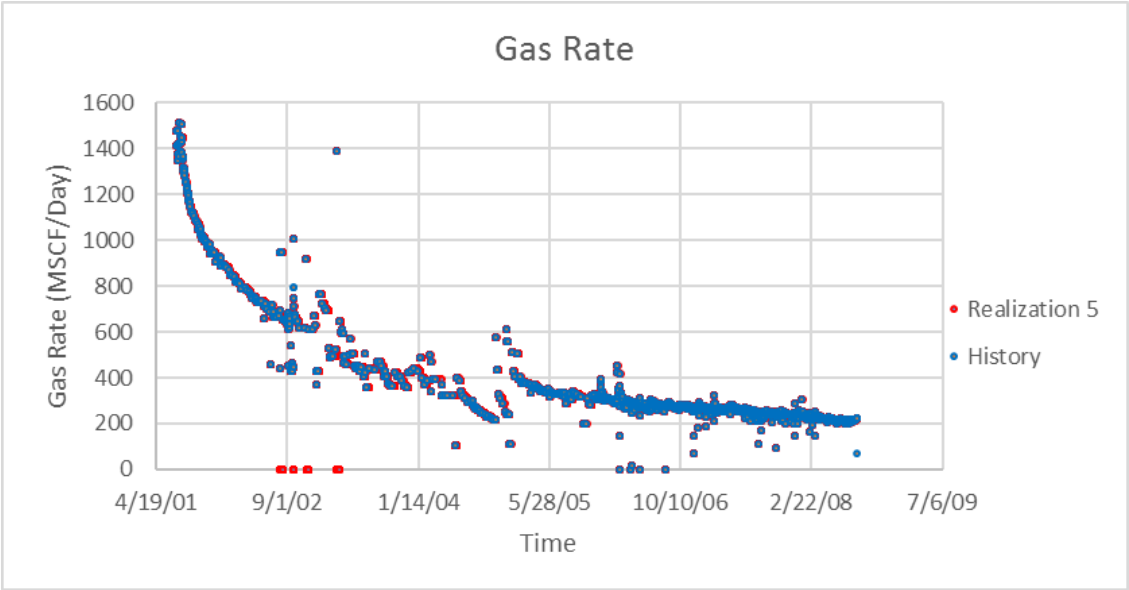

Figure 53: Gas rate of realization 5 versus production history.

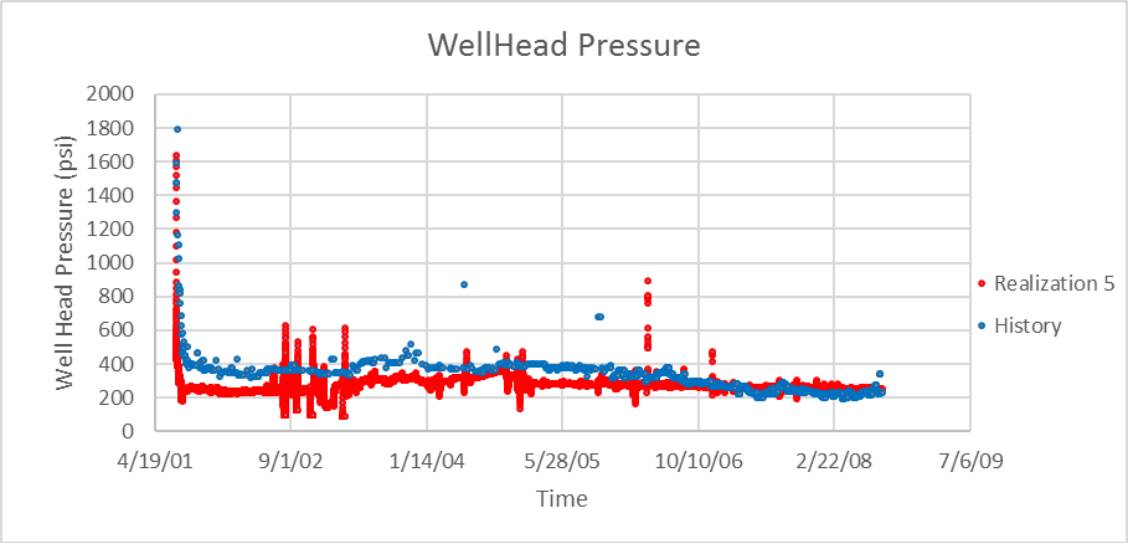

Figure 54: Wellhead pressure of realization 5 versus production history.

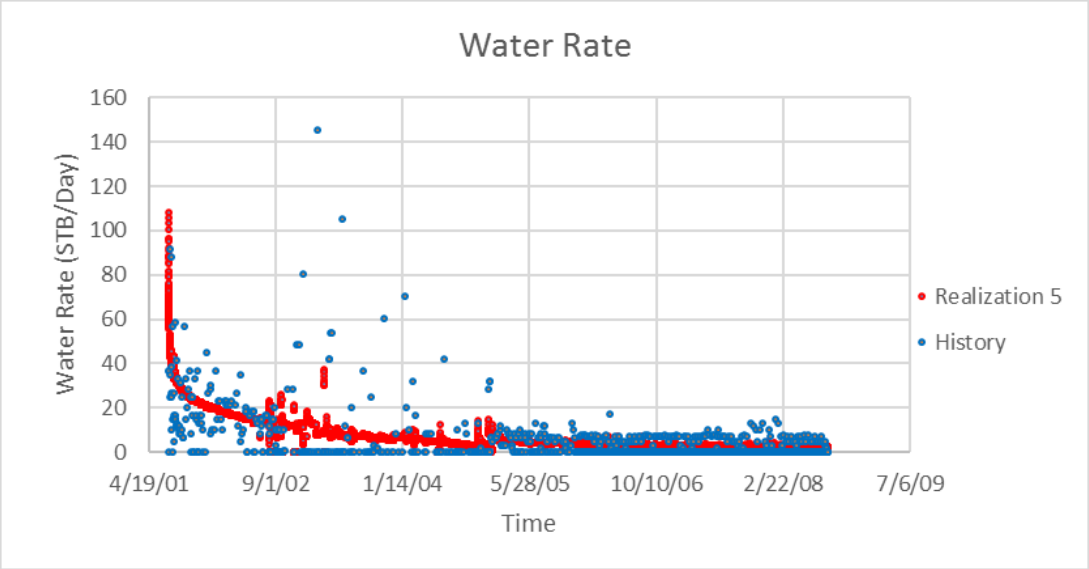

Figure 55: Water rate of realization 5 versus production history.

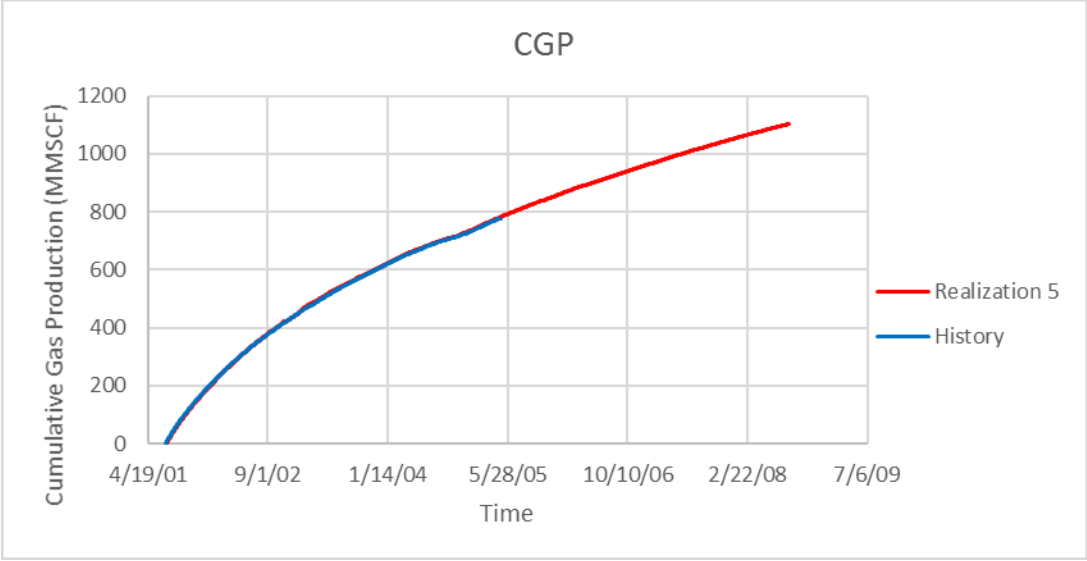

Figure 56: Cumulative gas production of realization 5 versus production history.

C: Hydraulics Table DESC Hydraulics Data

OGR 0

WGR 4e-003 8e-003 2e-002 5e-002 8e-002 0.11 0.14 0.2 0.25

QGAS 200.0 400.0 600.0 800.0 1000.0 1200.0 1400.0 1600.0

THP 300.0 600.0 900.0 1200.0 1500.0 1800.0

IOGR	IWGR	IQGAS	BHP(ITHP)					
1	1	1	431.785	968.864	1496.37	1995.77	2466.23	2908.91
1	2	1	540.6	1171.06	1734.22	2244.46	2714.07	3151.37
1	3	1	825.283	1533.13	2103.0	2601.98	3055.72	3476.84
1	4	1	1251.18	1941.97	2481.21	2951.73	3381.11	3782.01
1	5	1	1489.18	2147.8	2664.42	3118.23	3534.61	3925.2
1	6	1	1648.01	2281.13	2781.97	3224.56	3632.35	4016.26
1	7	1	1764.86	2378.05	2867.05	3301.25	3702.77	4081.9
1	8	1	1930.28	2514.09	2986.14	3408.64	3801.33	4173.66
1	9	1	2028.61	2594.64	3056.62	3472.1	3859.56	4227.89
1	1	2	395.025	876.656	1372.23	1856.0	2320.35	2761.85
1	2	2	462.309	1032.14	1574.53	2079.69	2551.16	2992.8
1	3	2	665.177	1345.63	1917.89	2425.43	2888.57	3318.47
1	4	2	1032.74	1741.11	2298.29	2783.8	3225.47	3636.33
1	5	2	1263.66	1951.98	2489.97	2959.62	3388.36	3788.75
1	6	2	1425.08	2092.24	2614.98	3073.33	3493.24	3886.6
1	7	2	1546.81	2195.46	2706.33	3156.07	3569.36	3957.55
1	8	2	1722.62	2342.2	2835.35	3272.57	3676.39	4057.31
1	9	2	1828.75	2429.8	2912.14	3341.84	3739.98	4116.5
1	1	3	381.579	835.73	1311.82	1784.1	2242.47	2681.79
1	2	3	431.254	965.286	1491.25	1989.95	2460.15	2902.81
1	3	3	591.765	1245.21	1813.5	2323.36	2790.5	3224.74
1	4	3	915.581	1624.6	2189.35	2682.65	3131.08	3547.71
1	5	3	1135.59	1835.44	2384.23	2862.8	3298.68	3704.89
1	6	3	1294.87	1977.88	2512.8	2980.33	3407.39	3806.47

1	7	3	1417.3	2084.07	2607.4	3066.26	3486.65	3880.42
1	8	3	1597.0	2236.16	2741.76	3187.99	3598.63	3984.78
1	9	3	1706.79	2327.69	2822.22	3260.57	3665.3	4046.93
1	1	4	374.812	811.953	1274.43	1737.91	2191.19	2628.15
1	2	4	414.637	924.419	1437.37	1930.05	2398.17	2840.76
1	3	4	548.999	1179.42	1742.3	2252.16	2721.37	3158.3
1	4	4	839.879	1543.81	2112.11	2610.11	3063.15	3483.63
1	5	4	1049.19	1752.95	2308.31	2792.71	3233.58	3643.83
1	6	4	1205.05	1896.24	2438.84	2912.58	3344.72	3747.89
1	7	4	1326.78	2003.77	2535.42	3000.72	3426.1	3823.88
1	8	4	1507.87	2159.19	2673.4	3125.91	3541.45	3931.45
1	9	4	1619.7	2253.2	2756.29	3200.91	3610.4	3995.69
1	1	5	370.956	796.26	1248.51	1704.92	2153.89	2588.57
1	2	5	404.443	896.422	1398.76	1886.09	2351.96	2793.95
1	3	5	521.049	1131.99	1689.08	2198.1	2668.44	3107.02
1	4	5	786.467	1482.89	2052.67	2553.8	3010.0	3433.49
1	5	5	986.07	1689.7	2249.14	2737.73	3182.31	3595.69
1	6	5	1138.19	1833.09	2380.96	2859.34	3295.25	3701.57
1	7	5	1258.65	1941.37	2478.93	2948.94	3378.2	3779.09
1	8	5	1439.94	2099.02	2619.44	3076.77	3496.1	3889.11
1	9	5	1552.95	2194.77	2704.24	3153.56	3566.75	3954.96
1	1	6	368.668	785.115	1229.3	1679.87	2125.07	2557.66
1	2	6	397.734	875.909	1369.3	1851.83	2315.51	2756.71
1	3	6	501.518	1095.78	1647.25	2154.88	2625.67	3065.44
1	4	6	746.803	1434.64	2004.66	2507.84	2966.53	3392.22
1	5	6	937.825	1638.9	2200.89	2692.67	3140.07	3555.95
1	6	6	1086.25	1781.99	2333.63	2815.48	3254.46	3663.23
1	7	6	1205.18	1890.71	2432.46	2906.2	3338.55	3741.96
1	8	6	1386.08	2049.79	2575.01	3036.1	3458.49	3853.95
1	9	6	1499.77	2146.97	2661.23	3114.34	3530.53	3921.11

1	1	7	367.345	776.823	1214.41	1660.02	2101.98	2532.62
1	2	7	393.158	860.2	1345.98	1824.14	2285.6	2726.0
1	3	7	487.289	1067.08	1613.14	2119.14	2590.0	3030.59
1	4	7	716.373	1395.17	1964.64	2469.24	2929.72	3357.24
1	5	7	899.868	1596.83	2160.35	2654.47	3104.2	3522.13
1	6	7	1044.81	1739.4	2293.57	2778.2	3219.65	3630.53
1	7	7	1162.17	1848.33	2393.21	2869.93	3304.74	3710.26
1	8	7	1342.33	2008.34	2537.28	3001.51	3426.38	3823.89
1	9	7	1456.39	2106.76	2624.71	3080.9	3499.58	3892.17
1	1	8	366.674	770.457	1202.5	1643.82	2082.83	2511.67
1	2	8	390.005	847.798	1326.95	1801.14	2260.49	2700.04
1	3	8	476.645	1043.71	1584.61	2088.84	2559.61	3000.68
1	4	8	692.512	1362.15	1930.52	2435.98	2897.9	3326.91
1	5	8	869.44	1561.25	2125.54	2621.45	3073.16	3492.72
1	6	8	1011.18	1703.18	2259.05	2745.87	3189.38	3602.04
1	7	8	1126.98	1812.16	2359.36	2838.37	3275.3	3682.61
1	8	8	1306.23	1972.91	2504.67	2971.37	3398.38	3797.65
1	9	8	1420.49	2072.19	2593.13	3051.8	3472.59	3866.89